

# SMART: spectral energy distributions Markov chain analysis with radiative transfer models

Charalambia Varnava ★ and Andreas Efstathiou ★

*School of Sciences, European University Cyprus, Diogenes street, Engomi, 1516 Nicosia, Cyprus*

Accepted 2024 April 25. Received 2024 April 24; in original form 2023 October 27

## ABSTRACT

In this paper we present the publicly available open-source spectral energy distribution (SED) fitting code SMART (Spectral energy distributions Markov chain Analysis with Radiative Transfer models). Implementing a Bayesian Markov chain Monte Carlo (MCMC) method, SMART fits the ultraviolet to millimetre SEDs of galaxies exclusively with radiative transfer models that currently constitute four types of pre-computed libraries, which describe the starburst, active galactic nucleus (AGN) torus, host galaxy, and polar dust components. An important novelty of SMART is that, although it fits SEDs exclusively with radiative transfer models, it takes comparable time to popular energy balance methods to run. Here we describe the key features of SMART and test it by fitting the multiwavelength SEDs of the 42 local ultraluminous infrared galaxies (ULIRGs) that constitute the HERschel Ultraluminous Infrared Galaxy Survey (HERUS) sample. The *Spitzer* spectroscopy data of the HERUS ULIRGs are included in the fitting at a spectral resolution, which is matched to that of the radiative transfer models. We also present other results that highlight the performance and versatility of SMART. SMART promises to be a useful tool for studying galaxy evolution in the *JWST* era. SMART is developed in PYTHON and is available at <https://github.com/ch-var/SMART.git>.

**Key words:** radiative transfer – galaxies: active – galaxies: interactions – quasars: general – infrared: galaxies – submillimetre: galaxies.

## 1 INTRODUCTION

One of the most important and challenging areas of research in modern Astrophysics concerns the study of the sequence of events that led to the formation of galaxies and the supermassive black holes (SMBHs) that usually reside at their centres. Understanding of the complex astrophysics that led to the observed distribution of galaxies, both in terms of properties and numbers, is usually sought within the framework of the standard  $\Lambda$  cold dark matter ( $\Lambda$ CDM) cosmological model (e.g. Lacey et al. 2016).

It is now clear that, in order to understand the numerous processes that govern galaxy formation and evolution (star formation in secular processes and in mergers, accretion onto SMBHs and feedback associated with them), we need multiwavelength or panchromatic observations of galaxies at all cosmic epochs. This is mainly due to the presence of cosmic dust in the interstellar medium (ISM) of galaxies, which significantly affects their ultraviolet (UV) to millimetre spectra. The necessity of characterizing the panchromatic emission of galaxies has led to a series of surveys at all wavelengths from X-ray to radio, of ever improving sensitivity, resolution, and sky coverage (Lonsdale et al. 2003; Eales et al. 2010; Oliver et al. 2012; Shirley et al. 2019, 2021). Most of these surveys can only be carried out from space, which has largely become possible over the last two or three decades with missions, such as IRAS, ISO, *Spitzer*, AKARI, Herschel, *Planck*, *WISE*, *GALEX*. At the same time,

significant progress has been made in the development of models. Stellar population synthesis (SPS) models (Bruzual & Charlot 1993, 2003; Maraston 2005; Conroy, Gunn & White 2009; Eldridge et al. 2017; Byrne et al. 2022) are an essential ingredient of models for the emission of galaxies. Another essential ingredient is a model for interstellar dust. Such models have been developed since the mid-80s (Draine & Lee 1984; Siebenmorgen & Krügel 1992; Draine & Li 2001; Li & Draine 2001, 2002; Jones et al. 2017; Hensley & Draine 2023).

The spectra of galaxies are usually decomposed into a number of components. It is widely acknowledged that radiative transfer models that include the effects of cosmic dust in a realistic geometry are needed for proper interpretation of the data and the self-consistent determination of a number of physical quantities of interest, such as the stellar mass of a galaxy, its current star formation rate (SFR) and active galactic nucleus (AGN) fraction. A number of radiative transfer models for the emission of starbursts, spheroidal and disc galaxies that take into account the effects of absorption, scattering, and re-emission by dust have been developed (Rowan-Robinson & Efstathiou 1993; Krügel & Siebenmorgen 1994; Silva et al. 1998; Efstathiou, Rowan-Robinson & Siebenmorgen 2000; Popescu et al. 2000, 2011, 2017; Siebenmorgen & Krügel 2007; Groves et al. 2008; Efstathiou & Siebenmorgen 2009; Camps & Baes 2020; Efstathiou et al. 2021). Following the development of the unified model for AGN (Antonucci & Miller 1985; Antonucci 1993), models for the emission of dusty tori of increasing degree of sophistication have been developed since the early-90s (Pier & Krolik 1992; Rowan-Robinson et al. 1993; Efstathiou & Rowan-Robinson 1995; Fritz,

\* E-mail: [varnava.haris@gmail.com](mailto:varnava.haris@gmail.com) (CV); [a.efstathiou@euc.ac.cy](mailto:a.efstathiou@euc.ac.cy) (AE)

Franceschini & Hatziminaoglou 2006; Siebenmorgen, Heymann & Efstathiou 2015; Stalevski et al. 2016; Hönig & Kishimoto 2017).

Model fitting techniques that can be used to aid the interpretation of multiwavelength observations of galaxies have also been developed (Efstathiou & Rowan-Robinson 2003; da Cunha, Charlot & Elbaz 2008; Noll et al. 2009; Chevillard & Charlot 2016; Eufrazio 2017; Carnall et al. 2018; Boquien et al. 2019; Johnson et al. 2021; Doore et al. 2023). However, the usual practice for the starburst and host galaxy components is to use approximate methods, such as energy balance. SED fitting results which incorporate radiative transfer models for the starburst and host galaxy component have so far been limited (Farrah et al. 2002, 2003; Verma et al. 2002; Vega et al. 2008; Herrero-Illana et al. 2017; Kankare et al. 2021; Efstathiou et al. 2022). A thorough review of spectral energy distribution (SED) fitting methods is given in Pacifici et al. (2023).

Our aim is to develop an SED fitting tool, which will allow fitting of the SEDs of local galaxies, for which rest frame mid-infrared (MIR) spectrophotometry from *Spitzer* and now *JWST* is available, but also for more distant galaxies, where more limited photometry is available. MIR spectrophotometry contains important features from dust, e.g. polycyclic aromatic hydrocarbon molecule (PAH) features and silicate features that are essential for constraining the energy source of galaxies (Efstathiou et al. 2022). Code Investigating GALaxy Emission (CIGALE; Noll et al. 2009; Boquien et al. 2019), being a grid-based method, only allows the specification of discrete values for the model parameters. This limits its ability to model spectrophotometry data, which are essential for decomposing the SEDs of galaxies and inferring the contribution of star formation and AGN activity. In our method we use the full range of the model parameters. This is particularly important for key parameters like the AGN torus inclination. Although CIGALE offers the option to add routines, we need a different concept to address our scientific aims. Paspaliaris et al. (2021) fitted luminous infrared galaxies (LIRGs) and ultraluminous infrared galaxies (ULIRGs) with CIGALE, but they did not include the *Spitzer* MIR spectrophotometry. This is also the case for the studies of Yang et al. (2020, 2022). We note that, of course, our method can also be applied to a broad range of high redshift galaxies with limited photometry, as we demonstrate in Section 4.5.

Considering all the above, we have developed a new method for fitting radiative transfer models to data, using a Markov chain Monte Carlo (MCMC) code: Spectral energy distributions Markov chain Analysis with Radiative Transfer models (SMART). We currently test SMART with a large sample of galaxies with excellent photometry and infrared (IR) spectrophotometry obtained with the Infrared Spectrograph (IRS) onboard the *Spitzer Space Telescope*. The novelty of SMART is that, although it utilizes exclusively radiative transfer models, it takes comparable time to popular energy balance methods.

In particular, we utilize four types of libraries of models as input to SMART for fitting the SEDs: these are the starburst (Efstathiou et al. 2000; Efstathiou & Siebenmorgen 2009), AGN torus (Efstathiou & Rowan-Robinson 1995; Fritz et al. 2006; Siebenmorgen et al. 2015; Stalevski et al. 2016), spheroidal (Efstathiou et al. 2021), or disc (Efstathiou, in preparation) host and polar dust (Efstathiou 2006) models. These libraries are part of the collection of radiative transfer models named CYprus models for Galaxies and their NUClear Spectra (CYGNUS). We have also added a component of polar dust in the fitting, which has been recognized as an important component in AGN since the mid-90s (see also Efstathiou, Hough & Young 1995; Efstathiou 2006; Mattila et al. 2018), and explore the use of other AGN torus models (e.g. Fritz et al. 2006; Siebenmorgen et al. 2015; Stalevski et al. 2016). As an MCMC sampler we utilize the publicly

available *emcee* code, which is a pure-PYTHON implementation of Goodman & Weare's (2010) Affine Invariant MCMC Ensemble sampler (Foreman-Mackey et al. 2013).

To test SMART, we fit the multiwavelength SEDs for the HERschel Ultraluminous Infrared Galaxy Survey (HERUS) sample (Farrah et al. 2013) at  $z < 0.27$ , assembled by Efstathiou et al. (2022). We are also testing SMART with other hyperluminous obscured galaxies at  $z > 4$ , such as the hyperluminous obscured quasar at  $z \sim 4.3$  discovered by Efstathiou et al. (2021) in the Herschel Extragalactic Legacy Project (HELP; Shirley et al. 2021). We fit the data with our method and the results of the fitting are then post-processed to derive physical quantities, such as stellar mass, SFR, starburst time-scale, AGN fraction etc., which are essential for studying galaxy evolution. In a companion paper Varnava & Efstathiou (in preparation) carry out a detailed study with SMART of the recently discovered hyperluminous infrared galaxy (HLIRG) COS-87529 at  $z = 6.853$  (Endsley et al. 2022). Efstathiou et al. (in preparation) use SMART to put constraints on the starburst and AGN activity of heavily obscured quasars at redshifts  $z \sim 0.3 - 3$  discovered by Lonsdale et al. (2015).

This paper is organized as follows: In Section 2 we describe our approach for SED fitting, in Section 3 we test our method with the HERUS sample, and in Section 4 we provide case studies to display the versatility of our method. In Section 5 we present our conclusions, as well as a few ideas for future development. Throughout this work we assume  $H_0 = 70 \text{ km s}^{-1} \text{ Mpc}^{-1}$ ,  $\Omega = 1$  and  $\Omega_\Lambda = 0.7$ .

## 2 OUR APPROACH

SMART demonstrates the feasibility of fitting the panchromatic SEDs of a large sample of galaxies exclusively with state-of-the-art radiative transfer models and extracting the important physical parameters. Efstathiou et al. (2021, 2022), as well as other previous studies by Herrero-Illana et al. (2017), Mattila et al. (2018), Kankare et al. (2021), presented results of SED fitting with radiative transfer models, using the IDL version of Spectral energy distribution Analysis Through Markov Chains (SATMC; Johnson et al. 2013) by employing the synthesis mode. SATMC by itself does not output physical quantities, such as stellar mass, SFRs, AGN fraction, and therefore additional post-processing routines were developed. More details of this approach are described in Efstathiou (in preparation).

In our method we address the need of developing an SED fitting code, which is specifically designed to fit efficiently galaxy SEDs, using exclusively radiative transfer models. We use the MCMC code *emcee* as the core of the method. The MCMC method, although computing intensive, gives the global best fit. In addition, as the method produces the posterior parameter distribution, realistic errors on the parameters can be estimated. This will motivate further work in using similar techniques to fit the panchromatic SEDs of the large samples of galaxies that have already been assembled by projects, such as HELP.

We fit the UV to millimetre SEDs with radiative transfer models that currently constitute four types of pre-computed libraries, which describe the starburst, AGN, host galaxy, and polar dust components. These four libraries are part of CYGNUS. The starburst and AGN models are assumed to be independent of redshift, whereas for the host galaxy a different library is selected depending on the redshift. SMART allows us to explore the impact of four different AGN models and therefore constrain the properties of the obscuring torus (more details are given in Efstathiou et al. 2022, see also Section 2.1).

The main novel features of our approach, which make it state-of-the-art in the field of SED fitting, are:

(i) SMART uses radiative transfer models that take properly into account the effects of dust in a realistic geometry, whereas popular energy balance methods, such as CIGALE (Noll et al. 2009; Boquien et al. 2019) and Multiwavelength Analysis of Galaxy Physical Properties (MAGPHYS; da Cunha et al. 2008), rely on various forms of attenuation laws. SMART can uniquely model a galaxy explicitly as a spheroidal or disc galaxy, whereas it takes comparable computing time to methods like CIGALE and MAGPHYS.

(ii) The code is paralllized and it is considerably faster than other MCMC codes, such as SATMC.

(iii) We make use of four different AGN libraries, as in Efstathiou et al. (2022).

(iv) As in Efstathiou et al. (2022), we can also optionally add a component of polar dust in the fitting.

(v) SMART is designed to fit an SED in comparable time with a spheroidal or disc host galaxy model.

(vi) With SMART we can fit part of a galaxy and, if necessary, switch off any of the four components (AGN torus, starburst, spheroidal/disc, polar dust).

SMART is an open-source and publicly available SED fitting code available at <https://github.com/ch-var/SMART.git>. A user manual with plenty of examples is also provided on the same website.

## 2.1 Description of the radiative transfer models

Our method relies on the availability of libraries of radiative transfer models for the emission of starburst episodes, AGN tori, and host galaxies. The models are part of the collection of radiative transfer models named CYGNUS.<sup>1</sup> The parameters of the models are listed in Table 1.

### 2.1.1 Starburst models

The starburst models currently included in CYGNUS were described in Efstathiou et al. (2000) and Efstathiou & Siebenmorgen (2009). Models for massive star formation and starbursts were also presented and discussed in Rowan-Robinson & Crawford (1989), Rowan-Robinson & Efstathiou (1993), Efstathiou & Rowan-Robinson (1994), Krügel & Siebenmorgen (1994), Silva et al. (1998), Takagi, Arimoto & Hanami (2003), Dopita et al. (2005), and Siebenmorgen & Krügel (2007). The starburst model assumes the following parameters, which have the range given in brackets: the age of the starburst ( $t_* = 5 - 35$  Myr), the giant molecular clouds' (GMCs') initial optical depth ( $\tau_v = 50 - 250$ ) and the time constant of the exponentially decaying SFR ( $\tau_* = 15 - 35$  Myr).

### 2.1.2 Spheroidal host models

The spheroidal host models are described in more detail in Efstathiou et al. (2021). The models of Bruzual & Charlot (1993, 2003) are used in combination with an assumed star formation history (SFH) to compute the spectrum of starlight, which is illuminating the dust throughout the model galaxy. The spectrum of starlight is assumed to be constant throughout the galaxy, but its intensity varies throughout the galaxy according to a Sérsic profile with  $n = 4$ , which is equivalent to de Vaucouleurs's law. Efstathiou & Rowan-Robinson (2003) assumed an exponentially decaying SFH, whereas here we

assume a delayed exponential ( $\dot{M}_* \propto t \times e^{-t/\tau^s}$ ), where  $\tau^s$  is the e-folding time of the exponential.

The spheroidal model assumes the following parameters, which have the range given in brackets: the e-folding time of the assumed delayed exponential SFH ( $\tau^s = 0.125 - 8$  Gyr), the optical depth of the galaxy from its centre to its surface ( $\tau_v^s = 0.1 - 15$ ) and a parameter that controls the bolometric intensity of stellar emission relative to that of the bolometric intensity of starlight in the solar neighbourhood ( $\psi^s = 1 - 17$ ). In this paper we use two libraries of spheroidal models, which were computed assuming an age for the galaxy equal to the age of the Universe at a redshift of  $z = 0.1$  and 4.3. We assumed that all the stars in the galaxy formed with a Salpeter Initial Mass Function (IMF) out of gas with a metallicity of 40 per cent of solar for the  $z = 0.1$  library and 6.5 per cent of solar for the  $z = 4.3$  library.

### 2.1.3 Disc host models

The disc models library has been computed with a 2D radiative transfer code that combines the features of the code of Efstathiou & Rowan-Robinson (1995) for modelling AGN tori, which does not include PAHs and small grains, and the spheroidal code of Efstathiou et al. (2021), which does. In the case of the disc models the distribution of stars, dust, and molecular clouds follows a double exponential (e.g. Silva et al. 1998) instead of the de Vaucouleurs's law assumed for the spheroidal models. The disc models have as parameters the disc SFR e-folding time  $\tau^d$ , the starlight intensity parameter  $\psi^d$ , and the equatorial optical depth in the V band  $\tau_v^d$ . Additionally, the disc models have the inclination of the disc as a parameter. The same dust model is used as in the case of the spheroidal models. The library used in this paper assumes that all the stars in the galaxy formed with a Salpeter IMF out of gas with a metallicity of 20 per cent of solar. The disc models have been used in Kool et al. (2018) and Kankare et al. (2021) to fit the SEDs of LIRGs. More details and applications of the disc models are given in Efstathiou (in preparation).

### 2.1.4 AGN torus models

There are a number of AGN torus models available in the literature, which make different assumptions about the obscurer geometry (Pier & Krolik 1993; Rowan-Robinson et al. 1993; Granato & Danese 1994; Efstathiou & Rowan-Robinson 1995; Nenkova et al. 2002, 2008; Dullemond & van Bemmell 2005; Fritz et al. 2006; Hönig et al. 2006; Schartmann et al. 2008; Heymann & Siebenmorgen 2012; Stalevski et al. 2012, 2016; Efstathiou et al. 2013; Siebenmorgen et al. 2015; Hönig & Kishimoto 2017). In SMART, we currently explore the impact of four different AGN models, which are described in more detail in Efstathiou et al. (2022):

(i) The CYGNUS AGN torus model. A number of results with this combination of models using the MCMC code SATMC have previously been presented (Herrero-Illana et al. 2017; Kool et al. 2018; Mattila et al. 2018; Pitchford et al. 2019; Efstathiou et al. 2021; Kankare et al. 2021; Efstathiou et al. 2022).

(ii) The AGN torus model of Fritz et al. (2006).

(iii) The two-phase AGN torus model SKIRTOR of Stalevski et al. (2016).

(iv) The two-phase AGN torus model of Siebenmorgen et al. (2015).

<sup>1</sup><https://arc.euc.ac.cy/cygnus-project-arc>

**Table 1.** Parameters of the models currently used in SMART, symbols used, their assumed ranges, and summary of other information about the models. In the Fritz et al. (2006) model there are two additional parameters that define the density distribution in the radial direction ( $\beta$ ) and azimuthal direction ( $\gamma$ ). In this paper we assume  $\beta = 0$  and  $\gamma = 4$ . In the SKIRTOR model there are two additional parameters that define the density distribution in the radial direction ( $p$ ) and azimuthal direction ( $q$ ). In this paper we assume  $p = 1$  and  $q = 1$ . In addition, the SKIRTOR library fixes the fraction of mass inside clumps to 97 per cent. There are four additional scaling parameters for the starburst, spheroidal or disc, AGN, and polar dust models,  $f_{\text{SB}}$ ,  $f_{\text{sph}}$  or  $f_{\text{disc}}$ ,  $f_{\text{AGN}}$ , and  $f_p$ , respectively.

Parameter	Symbol	Range	Comments
<b>CYGNUS Starburst</b>			
Initial optical depth of GMCs	$\tau_v$	50–250	Efstathiou et al. (2000), Efstathiou & Siebenmorgen (2009)
Starburst SFR e-folding time	$\tau_*$	10–35 Myr	Incorporates Bruzual & Charlot (1993), Bruzual & Charlot (2003)
Starburst age	$t_*$	5–35 Myr	Metallicity = solar, Salpeter IMF Standard galactic dust mixture with PAHs
<b>CYGNUS Spheroidal Host</b>			
Spheroidal SFR e-folding time	$\tau^s$	0.125–8 Gyr	Efstathiou & Rowan-Robinson (2003), Efstathiou et al. (2021)
Starlight intensity	$\psi^s$	1–17	Incorporates Bruzual & Charlot (1993), Bruzual & Charlot (2003)
Optical depth	$\tau_v^s$	0.1–15	Range of metallicities, Salpeter IMF Standard galactic dust mixture with PAHs
<b>CYGNUS Disc Host</b>			
Disc SFR e-folding time	$\tau^d$	0.5–8 Gyr	Efstathiou & Rowan-Robinson (2003), Efstathiou (in preparation)
Starlight intensity	$\psi^d$	1–9	Incorporates Bruzual & Charlot (1993), Bruzual & Charlot (2003)
Optical depth	$\tau_v^d$	0.1–29	Range of metallicities, Salpeter IMF
Inclination	$\theta_d$	0°–90°	Standard galactic dust mixture with PAHs
<b>CYGNUS AGN torus</b>			
Torus equatorial UV optical depth	$\tau_{uv}$	260–1490	Smooth tapered discs
Torus ratio of outer to inner radius	$r_2/r_1$	20–100	Efstathiou & Rowan-Robinson (1995), Efstathiou et al. (2013)
Torus half-opening angle	$\theta_o$	30°–75°	Standard galactic dust mixture without PAHs
Torus inclination	$\theta_i$	0°–90°	The subranges $\theta_o - 90^\circ$ and $0^\circ - \theta_o$ are assumed for AGN_type=2 and AGN_type = 1, respectively.
<b>Fritz et al. (2006) AGN torus</b>			
Torus equatorial optical depth at 9.7 $\mu\text{m}$	$\tau_{9.7 \mu\text{m}}$	1–10	Smooth flared discs
Torus ratio of outer to inner radius	$r_2/r_1$	10–150	Fritz et al. (2006)
Torus half-opening angle	$\theta_o$	20°–70°	Standard galactic dust mixture without PAHs
Torus inclination	$\theta_i$	0°–90°	The subranges $\theta_o - 90^\circ$ and $0^\circ - \theta_o$ are assumed for AGN_type=2 and AGN_type = 1, respectively.
<b>SKIRTOR AGN torus</b>			
Torus equatorial optical depth at 9.7 $\mu\text{m}$	$\tau_{9.7 \mu\text{m}}$	3–11	Two-phase flared discs
Torus ratio of outer to inner radius	$r_2/r_1$	10–30	Stalevski et al. (2012), Stalevski et al. (2016)
Torus half-opening angle	$\theta_o$	20°–70°	Standard galactic dust mixture without PAHs
Torus inclination	$\theta_i$	0°–90°	The subranges $\theta_o - 90^\circ$ and $0^\circ - \theta_o$ are assumed for AGN_type=2 and AGN_type = 1, respectively.
<b>Siebenmorgen et al. (2015) AGN torus</b>			
Cloud volume filling factor (per cent)	$V_c$	1.5–77	Two-phase anisotropic spheres
Optical depth of the individual clouds	$A_c$	0–45	Siebenmorgen et al. (2015)
Optical depth of the disc mid-plane	$A_d$	50–500	Fluffy dust mixture without PAHs
Inclination	$\theta_i$	0°–90°	The subranges 45°–90° and 0°–45° are assumed for AGN_type=2 and AGN_type = 1, respectively.
<b>Polar dust</b>			
Temperature	$T_p$	800 K–1200 K	Optically thick spherical clouds (Efstathiou 2006)

It is generally acknowledged in the literature (e.g. Efstathiou et al. 2014; Siebenmorgen et al. 2015; Efstathiou et al. 2022; García-Bernete et al. 2024) that clumpy and two-phase torus models cannot reproduce the deep silicate absorption features observed in objects like IRAS 08572+3915, which we discuss in Section 4.3 in detail. The parameter  $p$  in the SKIRTOR model takes four discrete values in the library (0, 0.5, 1, and 1.5). Assuming a value for  $p < 1$ , leads to AGN torus spectra with shallower silicate absorption features and therefore worse fits with these models. We have therefore fixed  $p$  to the value of 1. The parameter  $q$  in SKIRTOR concerns the azimuthal dependence of the density distribution and it is unlikely to have much impact on the silicate features. We have fixed this value at 1. The parameters of all of the AGN torus models used in this paper are summarized in Table 1.

### 2.1.5 Polar dust model

The model assumes that polar dust is concentrated in discrete spherical optically thick clouds, all of which are assumed to have constant temperature for all dust grains (Efstathiou 2006). The model assumes the same multigrain dust mixture as in the starburst radiative transfer model (Efstathiou & Siebenmorgen 2009), but the small grains and PAHs are assumed to be destroyed by the strong radiation field of the AGN to which these clouds are directly exposed. Unlike Efstathiou et al. (2022), in SMART the temperature of the polar dust clouds  $T_p$  is a free parameter in the fit and is assumed to vary in the range 800 K–1200 K. We assume that all clouds have an optical depth from the centre to the surface in the V band of 100.



## 2.2 Procedure for running SMART

We have developed the PYTHON routine *SMART* that makes a sequence of runs for different galaxies, which are selected from a list according to their flag. For example, in the following list we run the galaxies with flag = 1001:

name	redshift	flag	AGN_type
IRAS00188-0856	0.12840	1001	2
IRAS00397-1312	0.26170	1001	2
IRAS01003-2238	0.11780	1001	2
IRAS03158+4227	0.13440	1001	2
IRAS03521+0028	0.15190	1001	2
IRAS05189-2524	0.04256	1001	2
IRAS06035-7102	0.07947	1001	2
IRAS06206-6315	0.09244	1001	2
IRAS07598+6508	0.14830	1001	1
IRAS08311-2459	0.10040	1001	2
IRAS08572+3915	0.05835	1001	2
IRAS09022-3615	0.05964	1001	2
IRAS10378+1109	0.13620	1001	2
IRAS10565+2448	0.04300	1001	2
IRAS11095-0238	0.10660	1001	2
...			

The first column gives the name of the galaxy, which is also the name of the file that contains the data. The second column gives the redshift of the galaxy, the third column its selection flag, and the fourth column indicates whether the galaxy will be fitted with a type 1 or type 2 AGN torus model.

The fit for each galaxy takes  $\sim 2-3$  min on a machine with a few CPUs. but, because the code is parallelized, can run much faster on a supercomputer. SMART can optionally make a corner plot, in order to assess whether there are any degeneracies in the model parameters. For this plot we use the PYTHON package GETDIST (Lewis 2015), which we incorporate into SMART.

A number of physical quantities are extracted with the routine *post\_SMART* we have developed. The names of the physical quantities are self-explanatory, but we also list them and describe them briefly in Table 2.

## 2.3 Description of the post-processing routines

The PYTHON routine *post\_SMART* post-processes the output of the MCMC code. The user has the option to post-process the data generated by *SMART* for a number of galaxies, which are selected from a list according to their flag. The code gives the option to plot the residuals, which give an indication of the quality of the fit.

We have also developed the PYTHON routine *reformatter\_SMART* that reformats the output of SMART, in order to write the extracted physical quantities of the selected sample of galaxies, as well as their errors, in the form of a LaTeX table.

### 2.3.1 Calculation of luminosities and AGN fraction

SMART allows us to have the best-fitting spectrum for the total emission, as well as each of the four components of emission: starburst, AGN torus, host galaxy, and polar dust. We calculate the total luminosity, as well as that of each component separately, by integrating the spectra over the chosen wavelength range. All luminosities given in Table 2 are 1–1000  $\mu\text{m}$  luminosities. We can, of course, calculate the bolometric luminosities over the whole

**Table 2.** Derived physical quantities for the starburst, AGN torus, and host combination (spheroidal/disc), as well as the symbol used. The luminosities are integrated over 1–1000  $\mu\text{m}$ .

Physical quantity	Symbol
Observed AGN torus luminosity	$L_{\text{AGN}}^o$
Corrected AGN torus luminosity	$L_{\text{AGN}}^c$
Polar dust AGN luminosity	$L_p$
Starburst luminosity	$L_{\text{SB}}$
Spheroidal host luminosity	$L_{\text{sph}}$
Disc host luminosity	$L_{\text{disc}}$
Total observed luminosity	$L_{\text{tot}}^o$
Total corrected luminosity	$L_{\text{tot}}^c$
Starburst SFR (averaged over SB age)	$\dot{M}_{*}^{\text{age}}$
Spheroidal SFR	$\dot{M}_{\text{sph}}$
Disc SFR	$\dot{M}_{\text{disc}}$
Total SFR	$\dot{M}_{\text{tot}}$
Starburst stellar mass	$M_{\text{SB}}^{*}$
Spheroidal stellar mass	$M_{\text{sph}}^{*}$
Disc stellar mass	$M_{\text{disc}}^{*}$
Total stellar mass	$M_{\text{tot}}^{*}$
AGN fraction	$F_{\text{AGN}}$
Anisotropy correction factor	$A$

wavelength range covered by the models. Having calculated the total luminosity and that of the AGN torus, we can calculate the AGN fraction.

An important feature of the results from the SED fitting is that due to the anisotropy of the emission from the AGN torus, which is usually optically thick to its own radiation (Pier & Krolik 1993; Efstathiou & Rowan-Robinson 1995; Efstathiou et al. 2014), the AGN luminosity needs to be corrected by the anisotropy correction factor  $A(\theta_i)$  defined in Efstathiou (2006):

$$A(\theta_i) = \frac{\int_0^{\pi/2} S(\theta'_i) \sin\theta'_i d\theta'_i}{S(\theta_i)}, \quad (1)$$

where  $S(\theta_i)$  is the bolometric emission over the relevant wavelength range.  $A(\theta_i)$  is generally different for the IR and bolometric luminosities and is significant for all the AGN torus models considered here.

### 2.3.2 Calculation of SFRs and stellar mass

With SMART we can calculate separately the SFR and stellar mass of the starburst and the spheroidal or disc galaxy. All SFR and stellar mass estimates are calculated self-consistently, as the radiative transfer models used in the fits incorporate the SPS models of Bruzual & Charlot (1993, 2003).

Efstathiou et al. (2022) discussed two different estimates for the SFR of the starburst: the SFR averaged over the age of the starburst,  $\dot{M}_{*}^{\text{age}}$ , where the age is determined self-consistently from the fit, and the SFR averaged over a flat time-scale of 50 Myr,  $\dot{M}_{*}^{50}$ . Efstathiou et al. (2022) derived a very good relationship for the HERUS sample between the starburst luminosity and  $\dot{M}_{*}^{\text{age}}$ :

$$\frac{\dot{M}_{*}^{\text{age}}}{M_{\odot} \text{yr}^{-1}} = (3.11 \pm 0.05) \times 10^{-10} \frac{L_{\text{SB}}}{L_{\odot}}. \quad (2)$$

In the case of the spheroidal or disc component we are interested in the SFR at the time of observation. The SFR at all times of the history of the galaxy can, of course, be obtained from the assumed SFH, which takes the form of a delayed exponential.

### 2.3.3 Calculation of minimum reduced $\chi^2$

There is significant uncertainty in the models, which is primarily due to uncertainties regarding the dust properties, the geometry, numerical errors etc. The uncertainty in the observed photometry is primarily driven by the calibration uncertainty of the instruments. We therefore define the  $\chi^2$  statistic we use to compare the observed and the model SEDs as:

$$\chi^2 = \sum_n \left[ \frac{(y_n - \mu_n)^2}{(\sigma_\mu \mu_n)^2 + (\sigma_y y_n)^2} \right], \quad (3)$$

where  $y_n$  and  $\mu_n$  are the observed data and the corresponding model value, respectively,  $\sigma_\mu$  is the uncertainty of the model and  $\sigma_y$  is the uncertainty of the data.

Based on our analysis, in this paper we assumed that an uncertainty of 15 per cent realistically represented our confidence in the model SEDs. We also assumed 15 per cent of uncertainty in the observed photometry. The minimum reduced  $\chi^2$ ,  $\chi^2_{\min, \nu}$ , can then be obtained by  $\chi^2_{\min, \nu} = \frac{\chi^2_{\min}}{\nu}$ , where the degrees of freedom,  $\nu = n - m$ , equal the number of data points  $n$  minus the number of fitted parameters  $m$ .

## 3 TESTING SMART WITH THE HERUS SAMPLE

### 3.1 Sample details

The main sample of galaxies we will use for testing SMART is the HERUS sample (Farrah et al. 2013). This sample consists of 40 ULIRGs included in the Infrared Astronomical Satellite (IRAS) PSC-z survey (Saunders et al. 2000) with 60  $\mu\text{m}$  fluxes greater than 2 Jy. We also include three randomly selected ULIRGs with lower 60  $\mu\text{m}$  fluxes, IRAS 00397-1312 (1.8 Jy), IRAS 07598+6508 (1.7 Jy), and IRAS 13451+1232 (1.9 Jy). The quasar 3C 273 has been excluded, as it is a Blazar, to give a sample of 42 galaxies. The sample, strictly speaking, is not complete, but it includes nearly all known ULIRGs at  $z < 0.27$  and so provides an almost unbiased benchmark of local ULIRGs. All 42 galaxies were observed with the IRS instrument (Houck et al. 2004) on board *Spitzer* and by *Herschel*, as part of both the HERUS and SHINING surveys (Fischer et al. 2010; Sturm et al. 2011; Hailey-Dunsheath et al. 2012; González-Alfonso et al. 2013). HERUS studied some of the most luminous local ULIRGs, including famous objects like Arp 220, Mrk 231, and Mrk 273. In Fig. 1 we show the plot of the SFR against the total stellar mass for the 42 galaxies of the HERUS sample. In Fig. 2 we show the predicted contribution of starburst and AGN in the HERUS galaxies.

The multiwavelength photometry and how it was assembled is described in Efstathiou et al. (2022), but we summarize the approach here as well. The far-infrared (FIR) and submillimetre photometry refers to the whole galaxy, as the aperture is always larger than the size of the galaxies. This is also the case for the IRS spectroscopy, which has a slit width  $> 3.6$  arcsec that corresponds to a scale  $> 5$  kpc for a  $z > 0.1$  system in our sample. For the optical photometry we use the total aperture derived either from Pan-STARRS, SDSS, or from U et al. (2012). The IRS data included in the fits have a wavelength grid that is separated in steps of 0.05 in the log of the rest wavelength. We also add more points around the 9.7  $\mu\text{m}$  silicate feature and the PAH features to the equally spaced wavelength grid. The total number of data points we fitted varies from object to object. For example, in IRAS 03158+4227 we have a minimum of 30 data points, whereas in Arp 220 we have a maximum number of 55 data points. There is

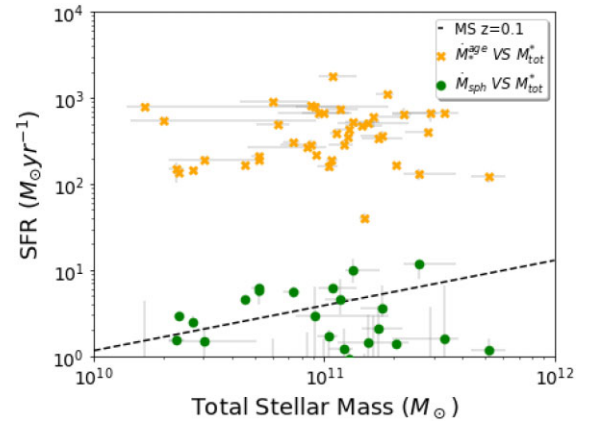


**Figure 1.** Starburst or host SFR against total stellar mass for the HERUS sample. Also plotted is the SFR–stellar mass ( $\dot{M}_* - M_*$ ) ‘main-sequence’ relation at  $z = 0.1$ , calculated via equation (28) of Speagle et al. (2014) with  $t = 12.161$  Gyr being the age of the Universe at  $z = 0.1$  for the assumed cosmology.

only one ULIRG in our sample with clear signs of a type 1 AGN and we discuss this object in detail in Section 4.2.

### 3.2 Results for the HERUS sample

In this subsection, we present the results of fitting the HERUS sample with SMART. For most of the objects the fits are satisfactory and of similar quality as in the fits with SATMC reported in Efstathiou et al. (2022). Tables A1 and A2 give selected fitted parameters, along with their errors, of the HERUS sample of 42 local ULIRGs, using the CYGNUS radiative transfer models for starbursts, AGN tori, host galaxies, and polar dust. In Figs A1, A2, A3, A4, A5, and A6 we present the UV to millimetre SED fits of the HERUS sample. The quality of the fits is demonstrated by a plot of the distribution of the reduced  $\chi^2$  shown in Fig. 3. We note that the distribution peaks at  $\sim 1.75$  and, apart from the fit of Arp 220 which has  $\chi^2_{\min, \nu} = 5.23$ , the fits for all other galaxies provide  $\chi^2_{\min, \nu} < 3.16$ . The values of the reduced  $\chi^2$  are, of course, sensitive to the assumed values of  $\sigma_\mu$  and  $\sigma_y$  in equation (3). Tables 3 and 4 give the extracted physical quantities, as well as their errors. An example of a corner plot is shown in Fig. 4 for the SED fit of IRAS 05189-2524, which we discuss in more detail in Section 4.1. For this corner plot we omit some nuisance parameters (our scaling parameters) to make the rest of them more visible.

There are two ULIRGs (IRAS 01003–2238 and Mrk 1014) for which the fit is unsatisfactory, despite repeated runs of the code. As also noted by Efstathiou et al. (2022), in these objects there is most probably a dual AGN, one viewed with its torus edge-on and dominating in the MIR, and one viewed face-on, which dominates in the optical/UV. We have not developed yet SMART to deal with the case of dual AGN, so in Figs A1 and A5 we plot the fit with a single AGN.

For three of the ULIRGs plotted in Figs A1, A2, and A3 we run the code with polar dust enabled, as we see evidence that the addition of polar dust can improve the fit. These are IRAS 05189–2524, IRAS 07598+6508, and IRAS 13451+1232. We discuss IRAS 05189–2524 and IRAS 07598+6508 in more detail in Sections 4.1 and 4.2, respectively.

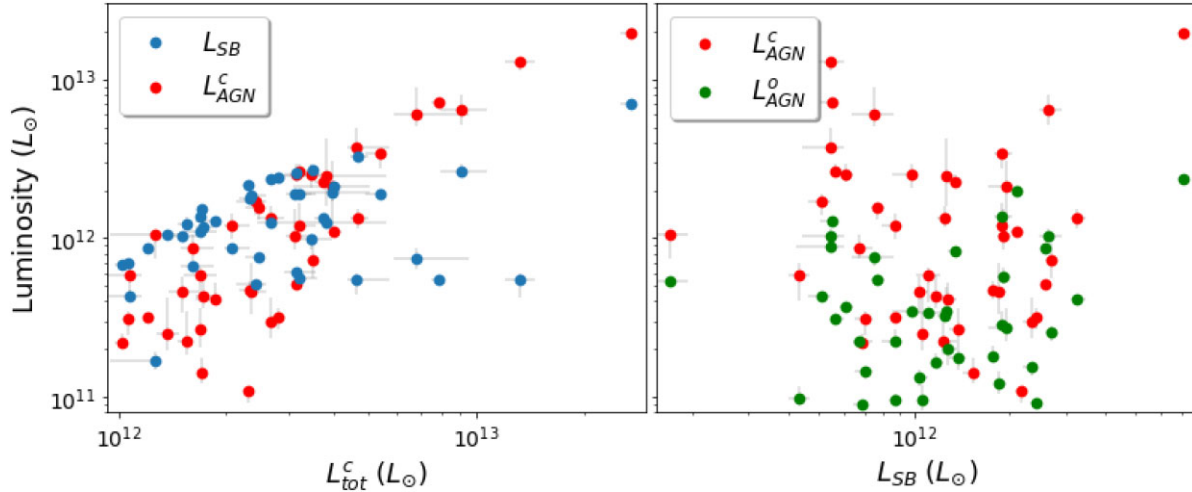


**Figure 2.** *Left:* Starburst and anisotropy-corrected AGN luminosity against total corrected IR luminosity. The starburst usually dominates the IR emission, except at  $L_{\text{tot}}^c \gtrsim 3 \times 10^{12} L_{\odot}$  when AGNs start to make a significant or dominant contribution. *Right:* Observed and anisotropy-corrected AGN luminosity against starburst luminosity. There is no clear evidence of a relation between  $L_{\text{SB}}$  and  $L_{\text{AGN}}$ .

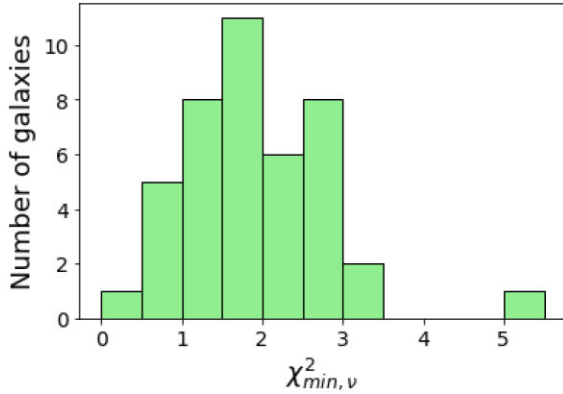


**Figure 3.** Distribution of the reduced  $\chi^2$  for the galaxies of the HERUS sample, which shows that almost all the fits have  $\chi_{\text{min},\nu}^2 \leq 3.5$ . The exception is Arp 220.

### 3.3 Comparison with results from other approaches

In Fig. 5 we compare key physical quantities derived by SMART with those obtained with SATMC, using the same multicomponent CYGNUS radiative transfer models as in Efstathiou et al. (2022). Regarding the luminosity and the SFR of the starburst, we see that there is very good agreement between the estimates of SMART and SATMC, with only a few exceptions. Some of the exceptions may be attributed to the statistical nature of the methods and this issue certainly deserves further exploration to understand these differences better. The corresponding comparison for the observed AGN torus luminosity shows that there is generally good agreement between the estimates with SMART and SATMC. For the AGN fraction, as expected, there is more discrepancy. We attribute the more scatter in the AGN fraction to the fact that it incorporates the anisotropy corrections, so it is much more sensitive to changes to best-fitting parameters compared to other quantities, such as the luminosity of the starburst, the SFR of the starburst, and the observed AGN torus luminosity. We conclude that for most of the galaxies the fits with SMART are satisfactory and of similar quality as in the fits with SATMC reported in Efstathiou et al. (2022). It is, however, important to note that, even using the same models, significant differences can

arise in key physical quantities due to the statistical nature of the SED fitting methods.

Eleven of the sources in the sample of Paspaliaris et al. (2021) are ULIRGs and seven of them are included in the HERUS sample. We compare the results of Paspaliaris et al. (2021) obtained with CIGALE and using the SKIRTOR AGN torus model with those obtained with our method in Fig. 5. We observe good agreement in the SFR predicted by SMART and CIGALE. The only exception is IRAS 08572+3915 for which CIGALE predicts a much lower SFR. This is the galaxy we discuss in detail in Section 4.3. The model of Paspaliaris et al. (2021) fails to reproduce the deep silicate absorption feature of this ULIRG, which in our model is attributed to the fact that the smooth AGN torus is viewed almost edge-on. It is well understood that two-phase models like SKIRTOR cannot produce deep silicate absorption features like the one observed in IRAS 08572+3915 (see, for example, discussion in Efstathiou et al. 2022). The results of Paspaliaris et al. (2021) do not take into account the anisotropy correction and this is probably one of the main reasons the AGN fraction of the seven ULIRGs in common with our sample are lower.

## 4 DISCUSSION

In this section we discuss the versatility of SMART by providing a number of case studies. As part of this demonstration, we present a set of SED fits derived from SMART and highlighting the key advantages of the method. All of the following SED fits are done with the CYGNUS multicomponent radiative transfer models. In Sections 4.3 and 4.5 we present a comparison of our results for the galaxies IRAS 08572+3915 and HELP J100156.75+022344.7, respectively, with the other AGN models that we have available (the smooth torus model of Fritz et al. 2006 and the two-phase models of Siebenmorgen et al. 2015 and SKIRTOR).

### 4.1 Fit of a ULIRG associated with polar dust

IRAS 05189–2524 is generally believed to be a ‘warm’ ULIRG and to contain an obscured AGN with its torus viewed almost edge-on. This galaxy was recognized from the mid-90s as a ULIRG that has similar characteristics to the prototypical Seyfert 2 galaxy NGC 1068.

**Table 3.** Selected extracted physical quantities for the galaxies in the HERUS sample. For the AGN and total luminosities the anisotropy-corrected luminosities are given. All of the luminosities are 1–1000  $\mu\text{m}$  luminosities.

Name	$z$	$L_{\text{AGN}}^c$ $10^{12} L_{\odot}$	$L_{\text{SB}}$ $10^{11} L_{\odot}$	$L_{\text{sph}}$ $10^{10} L_{\odot}$	$L_p$ $10^{10} L_{\odot}$	$L_{\text{tot}}^c$ $10^{12} L_{\odot}$	$\dot{M}_{*}^{\text{age}}$ $M_{\odot} \text{ yr}^{-1}$	$\dot{M}_{\text{sph}}$ $M_{\odot} \text{ yr}^{-1}$
IRAS00188–0856	0.12840001	$0.43^{+0.11}_{-0.1}$	$17.63^{+0.88}_{-0.48}$	$3.47^{+8.95}_{-0.09}$	–	$2.27^{+0.14}_{-0.15}$	$592.6^{+7.1}_{-69.36}$	$0.24^{+2.71}_{-0.05}$
IRAS00397–1312	0.2617	$19.42^{+1.85}_{-1.52}$	$69.97^{+5.4}_{-2.61}$	$5.39^{+0.63}_{-0.31}$	–	$26.25^{+1.97}_{-1.1}$	$1822.0^{+107.8}_{-170.2}$	$6.17^{+0.63}_{-0.8}$
IRAS01003–2238	0.1178	$7.07^{+0.25}_{-0.39}$	$5.56^{+0.13}_{-0.5}$	$2.3^{+0.14}_{-0.37}$	–	$7.6^{+0.29}_{-0.34}$	$134.8^{+10.72}_{-8.25}$	$2.94^{+0.05}_{-0.44}$
IRAS03158+4227	0.1344	$6.61^{+1.48}_{-1.22}$	$26.49^{+3.6}_{-1.41}$	$1.35^{+1.71}_{-0.58}$	–	$9.26^{+1.38}_{-1.14}$	$904.6^{+37.53}_{-41.98}$	$0.42^{+2.44}_{-0.42}$
IRAS03521+0028	0.1519	$1.98^{+0.93}_{-0.82}$	$19.51^{+0.79}_{-2.43}$	$1.84^{+1.25}_{-0.5}$	–	$3.91^{+1.06}_{-0.83}$	$667.3^{+33.28}_{-95.5}$	$0.0^{+0.0}_{-0.0}$
IRAS05189–2524	0.04256	$1.57^{+0.08}_{-0.27}$	$7.61^{+0.47}_{-0.3}$	$2.6^{+0.17}_{-0.16}$	$10.76^{+1.47}_{-0.85}$	$2.46^{+0.08}_{-0.2}$	$191.8^{+9.85}_{-9.97}$	$0.29^{+0.03}_{-0.04}$
IRAS06035–7102	0.07947	$0.4^{+0.06}_{-0.06}$	$12.74^{+0.77}_{-0.54}$	$9.7^{+1.8}_{-5.87}$	–	$1.82^{+0.05}_{-0.19}$	$342.8^{+41.24}_{-32.88}$	$2.14^{+1.73}_{-2.14}$
IRAS06206–6315	0.09244	$0.5^{+0.08}_{-0.11}$	$11.7^{+0.52}_{-0.39}$	$8.4^{+0.82}_{-2.52}$	–	$1.78^{+0.06}_{-0.12}$	$396.7^{+42.52}_{-41.45}$	$0.0^{+0.01}_{-0.0}$
IRAS07598+6508	0.1483	$1.11^{+0.04}_{-0.07}$	$21.32^{+0.77}_{-1.32}$	$0.29^{+3.27}_{-0.28}$	$84.17^{+7.89}_{-19.47}$	$4.02^{+0.14}_{-0.16}$	$546.5^{+39.41}_{-36.79}$	$0.0^{+0.19}_{-0.0}$
IRAS08311–2459	0.1004	$1.03^{+0.46}_{-0.23}$	$19.02^{+1.48}_{-0.81}$	$8.77^{+0.75}_{-0.69}$	–	$3.08^{+0.38}_{-0.15}$	$663.6^{+70.47}_{-38.99}$	$1.59^{+4.81}_{-1.52}$
IRAS08572+3915	0.05835	$12.85^{+1.1}_{-1.36}$	$5.46^{+0.42}_{-1.07}$	$1.67^{+0.08}_{-0.09}$	–	$13.34^{+1.21}_{-1.4}$	$154.0^{+17.93}_{-48.26}$	$1.52^{+0.15}_{-0.13}$
IRAS09022–3615	0.05964	$0.26^{+0.13}_{-0.06}$	$13.75^{+0.75}_{-0.63}$	$3.6^{+0.51}_{-0.55}$	–	$1.69^{+0.08}_{-0.05}$	$471.6^{+12.54}_{-21.13}$	$0.41^{+0.08}_{-0.08}$
IRAS10378+1109	0.1362	$2.35^{+1.57}_{-0.74}$	$12.68^{+0.46}_{-0.54}$	$3.59^{+0.49}_{-0.26}$	–	$3.68^{+1.54}_{-0.81}$	$435.9^{+25.88}_{-43.45}$	$1.01^{+0.21}_{-0.18}$
IRAS10565+2448	0.043	$0.32^{+0.02}_{-0.02}$	$8.64^{+0.32}_{-0.27}$	$2.07^{+0.13}_{-0.08}$	–	$1.21^{+0.03}_{-0.04}$	$395.6^{+13.46}_{-13.02}$	$0.0^{+0.01}_{-0.0}$
IRAS11095–0238	0.1066	$6.17^{+3.61}_{-0.88}$	$7.65^{+0.84}_{-1.32}$	$1.72^{+1.65}_{-0.36}$	–	$7.03^{+3.35}_{-0.92}$	$186.3^{+27.94}_{-17.52}$	$1.49^{+0.71}_{-0.59}$
IRAS12071–0444	0.1284	$2.22^{+0.32}_{-0.1}$	$13.46^{+0.06}_{-0.7}$	$8.4^{+2.91}_{-3.0}$	–	$3.65^{+0.11}_{-0.12}$	$362.8^{+44.48}_{-36.01}$	$2.89^{+3.74}_{-0.89}$
IRAS13120–5453	0.03076	$0.15^{+0.03}_{-0.01}$	$14.83^{+0.77}_{-0.91}$	$2.85^{+1.38}_{-0.66}$	–	$1.67^{+0.06}_{-0.05}$	$658.9^{+40.2}_{-47.42}$	$0.86^{+1.11}_{-0.64}$
IRAS13451+1232	0.1217	$3.73^{+1.26}_{-0.19}$	$5.5^{+0.5}_{-1.06}$	$23.45^{+0.54}_{-0.42}$	$4.23^{+2.99}_{-1.24}$	$4.59^{+1.12}_{-0.24}$	$131.7^{+18.56}_{-22.22}$	$11.79^{+1.02}_{-3.94}$
IRAS14348–1447	0.0827	$0.45^{+0.25}_{-0.12}$	$18.49^{+1.0}_{-0.46}$	$4.74^{+1.5}_{-0.21}$	–	$2.35^{+0.28}_{-0.09}$	$512.6^{+49.4}_{-29.2}$	$1.67^{+1.33}_{-1.6}$
IRAS14378–3651	0.0676	$0.46^{+0.08}_{-0.12}$	$10.18^{+0.5}_{-0.2}$	$2.1^{+1.88}_{-0.6}$	–	$1.47^{+0.21}_{-0.12}$	$287.7^{+36.94}_{-21.34}$	$0.02^{+0.63}_{-0.01}$
IRAS15250+3609	0.05516	$2.54^{+0.55}_{-0.25}$	$5.98^{+0.56}_{-0.4}$	$2.15^{+0.33}_{-0.11}$	–	$3.18^{+0.41}_{-0.28}$	$144.8^{+9.01}_{-9.26}$	$2.48^{+0.19}_{-0.1}$
IRAS15462–0450	0.09979	$0.6^{+0.16}_{-0.2}$	$11.49^{+0.69}_{-1.5}$	$2.36^{+0.31}_{-0.25}$	–	$1.72^{+0.22}_{-0.18}$	$268.0^{+10.33}_{-16.77}$	$0.73^{+1.17}_{-0.71}$
IRAS16090–0139	0.13358	$0.72^{+0.18}_{-0.16}$	$27.05^{+0.86}_{-0.8}$	$3.98^{+2.82}_{-0.81}$	–	$3.48^{+0.12}_{-0.13}$	$780.6^{+76.4}_{-42.66}$	$2.56^{+2.89}_{-2.56}$
IRAS17208–0014	0.0428	$0.11^{+0.0}_{-0.02}$	$21.66^{+0.97}_{-0.78}$	$1.57^{+0.1}_{-0.02}$	–	$2.29^{+0.08}_{-0.08}$	$809.4^{+68.56}_{-30.52}$	$0.19^{+0.59}_{-0.08}$
IRAS19254–7245	0.061709	$1.73^{+0.63}_{-0.32}$	$5.06^{+0.39}_{-0.66}$	$19.09^{+5.14}_{-2.12}$	–	$2.45^{+0.52}_{-0.31}$	$119.7^{+6.24}_{-14.92}$	$1.08^{+0.45}_{-0.3}$
IRAS19297–0406	0.08573	$0.31^{+0.13}_{-0.08}$	$23.3^{+0.37}_{-1.78}$	$4.1^{+0.11}_{-0.08}$	–	$2.66^{+0.04}_{-0.06}$	$660.0^{+113.1}_{-21.46}$	$0.0^{+0.42}_{-0.0}$
IRAS20087–0308	0.10567	$0.33^{+0.04}_{-0.04}$	$23.99^{+0.74}_{-1.1}$	$3.65^{+0.78}_{-0.46}$	–	$2.77^{+0.05}_{-0.08}$	$1108.0^{+33.86}_{-59.3}$	$0.0^{+0.27}_{-0.0}$
IRAS20100–4156	0.12958	$1.3^{+0.18}_{-0.17}$	$32.62^{+1.63}_{-1.06}$	$6.27^{+5.04}_{-0.9}$	–	$4.65^{+0.26}_{-0.25}$	$763.1^{+43.59}_{-50.99}$	$4.56^{+3.76}_{-0.94}$
IRAS20414–1651	0.087084	$0.22^{+0.12}_{-0.04}$	$12.35^{+1.23}_{-0.23}$	$1.31^{+0.04}_{-0.07}$	–	$1.56^{+0.01}_{-0.09}$	$495.1^{+72.17}_{-4.58}$	$0.18^{+0.34}_{-0.07}$
IRAS20551–4250	0.042996	$0.84^{+0.18}_{-0.11}$	$6.65^{+0.63}_{-0.43}$	$4.85^{+0.73}_{-0.41}$	–	$1.56^{+0.18}_{-0.13}$	$163.6^{+20.84}_{-11.2}$	$4.64^{+0.38}_{-0.4}$
IRAS22491–1808	0.0778	$1.13^{+1.15}_{-0.17}$	$8.39^{+0.72}_{-1.2}$	$7.9^{+0.3}_{-4.03}$	–	$2.07^{+1.13}_{-0.2}$	$209.5^{+21.62}_{-46.27}$	$6.27^{+0.29}_{-2.25}$
IRAS23128–5919	0.0446	$0.3^{+0.04}_{-0.04}$	$6.95^{+0.39}_{-0.43}$	$5.48^{+1.56}_{-0.66}$	–	$1.06^{+0.03}_{-0.06}$	$187.5^{+8.98}_{-17.01}$	$5.61^{+0.74}_{-0.88}$
IRAS23230–6926	0.10659	$1.33^{+0.27}_{-0.15}$	$12.28^{+0.56}_{-0.81}$	$9.41^{+0.57}_{-1.79}$	–	$2.62^{+0.27}_{-0.13}$	$303.4^{+10.07}_{-14.64}$	$5.74^{+0.56}_{-0.96}$
IRAS23253–5415	0.13	$1.16^{+0.2}_{-0.07}$	$19.08^{+0.67}_{-0.95}$	$6.83^{+0.74}_{-0.83}$	–	$3.18^{+0.09}_{-0.11}$	$674.3^{+52.35}_{-80.31}$	$0.82^{+3.14}_{-0.79}$
IRAS23365+3604	0.0645	$2.63^{+0.37}_{-0.54}$	$9.84^{+1.34}_{-1.28}$	$5.64^{+1.21}_{-2.14}$	–	$3.61^{+0.54}_{-0.47}$	$285.7^{+101.3}_{-21.5}$	$1.22^{+1.32}_{-0.73}$
Mrk1014	0.16311	$0.51^{+0.02}_{-0.04}$	$25.87^{+0.99}_{-1.4}$	$0.01^{+6.39}_{-0.01}$	–	$3.12^{+0.09}_{-0.13}$	$787.1^{+49.55}_{-62.5}$	$0.0^{+4.95}_{-0.0}$
UGC5101	0.039367	$0.22^{+0.04}_{-0.02}$	$6.85^{+0.31}_{-0.24}$	$11.25^{+0.36}_{-0.45}$	–	$1.02^{+0.03}_{-0.03}$	$168.6^{+9.03}_{-8.99}$	$1.43^{+0.08}_{-0.14}$
Mrk231	0.04217	$3.4^{+0.38}_{-0.62}$	$18.75^{+1.6}_{-0.65}$	$10.23^{+3.05}_{-1.23}$	–	$5.35^{+0.44}_{-0.37}$	$515.5^{+33.35}_{-37.06}$	$10.58^{+2.95}_{-3.16}$
Mrk273	0.03778	$0.26^{+0.13}_{-0.04}$	$10.54^{+0.43}_{-0.44}$	$3.52^{+0.29}_{-0.25}$	–	$1.38^{+0.1}_{-0.08}$	$356.0^{+17.54}_{-14.23}$	$0.46^{+0.1}_{-0.1}$
Mrk463	0.050355	$1.05^{+0.05}_{-0.3}$	$1.7^{+0.24}_{-0.23}$	$3.78^{+0.83}_{-0.55}$	–	$1.26^{+0.02}_{-0.32}$	$40.28^{+5.74}_{-5.5}$	$0.05^{+1.01}_{-0.04}$
Arp220	0.018	$2.6^{+0.34}_{-0.29}$	$5.71^{+0.3}_{-0.22}$	$1.93^{+0.04}_{-0.04}$	–	$3.2^{+0.38}_{-0.26}$	$216.8^{+4.27}_{-12.76}$	$0.03^{+0.01}_{-0.0}$
NGC6240	0.0244	$0.59^{+0.13}_{-0.19}$	$4.33^{+0.3}_{-0.29}$	$4.89^{+0.78}_{-1.06}$	–	$1.08^{+0.15}_{-0.17}$	$162.5^{+19.42}_{-22.86}$	$1.48^{+0.44}_{-0.65}$



**Table 4.** Other extracted physical quantities for the galaxies in the HERUS sample.

Name	$\dot{M}_{\text{tot}}$ $\text{M}_{\odot} \text{ yr}^{-1}$	$M_{\text{sp}}^*$ $10^{10} \text{ M}_{\odot}$	$M_{\text{SB}}^*$ $10^9 \text{ M}_{\odot}$	$M_{\text{tot}}^*$ $10^{10} \text{ M}_{\odot}$	$F_{\text{AGN}}$	$A$
IRAS00188–0856	592.8 <sup>7.29</sup> <sub>–65.63</sub>	14.44 <sup>2.94</sup> <sub>–0.13</sub>	17.25 <sup>0.03</sup> <sub>–3.02</sub>	16.16 <sup>2.64</sup> <sub>–0.2</sub>	0.19 <sup>0.03</sup> <sub>–0.04</sub>	2.48 <sup>0.37</sup> <sub>–0.26</sub>
IRAS00397–1312	1827.0 <sup>109.7</sup> <sub>–169.2</sub>	9.7 <sup>2.66</sup> <sub>–1.79</sub>	13.19 <sup>1.34</sup> <sub>–1.91</sub>	11.03 <sup>2.79</sup> <sub>–1.72</sub>	0.73 <sup>0.03</sup> <sub>–0.02</sub>	8.26 <sup>0.24</sup> <sub>–0.3</sub>
IRAS01003–2238	137.6 <sup>10.41</sup> <sub>–8.06</sub>	2.21 <sup>0.06</sup> <sub>–0.27</sub>	1.74 <sup>1.11</sup> <sub>–0.25</sub>	2.35 <sup>0.09</sup> <sub>–0.13</sub>	0.93 <sup>0.0</sup> <sub>–0.01</sub>	5.57 <sup>0.1</sup> <sub>–0.06</sub>
IRAS03158+4227	907.5 <sup>34.95</sup> <sub>–44.92</sub>	4.0 <sup>3.42</sup> <sub>–1.96</sub>	24.02 <sup>2.03</sup> <sub>–2.02</sub>	6.31 <sup>3.59</sup> <sub>–1.74</sub>	0.7 <sup>0.05</sup> <sub>–0.04</sub>	6.43 <sup>0.8</sup> <sub>–1.01</sub>
IRAS03521+0028	667.3 <sup>33.28</sup> <sub>–95.5</sub>	7.96 <sup>3.06</sup> <sub>–1.55</sub>	19.9 <sup>1.03</sup> <sub>–2.48</sub>	9.94 <sup>3.17</sup> <sub>–1.44</sub>	0.51 <sup>0.08</sup> <sub>–0.13</sub>	7.67 <sup>0.87</sup> <sub>–2.51</sub>
IRAS05189–2524	192.2 <sup>9.78</sup> <sub>–10.01</sub>	10.42 <sup>0.55</sup> <sub>–0.53</sub>	3.79 <sup>0.76</sup> <sub>–0.56</sub>	10.79 <sup>0.64</sup> <sub>–0.55</sub>	0.63 <sup>0.02</sup> <sub>–0.06</sub>	2.89 <sup>0.08</sup> <sub>–0.06</sub>
IRAS06035–7102	344.6 <sup>39.43</sup> <sub>–30.82</sub>	16.99 <sup>4.01</sup> <sub>–2.43</sub>	2.68 <sup>7.38</sup> <sub>–0.45</sub>	17.41 <sup>4.51</sup> <sub>–2.6</sub>	0.22 <sup>0.03</sup> <sub>–0.02</sub>	2.13 <sup>0.34</sup> <sub>–0.13</sub>
IRAS06206–6315	396.7 <sup>42.52</sup> <sub>–41.45</sub>	26.0 <sup>2.22</sup> <sub>–3.49</sub>	10.83 <sup>2.07</sup> <sub>–1.05</sub>	27.07 <sup>1.88</sup> <sub>–3.1</sub>	0.28 <sup>0.04</sup> <sub>–0.05</sub>	2.88 <sup>0.45</sup> <sub>–0.4</sub>
IRAS07598+6508	546.8 <sup>39.19</sup> <sub>–36.99</sub>	0.96 <sup>8.73</sup> <sub>–0.92</sub>	13.51 <sup>1.63</sup> <sub>–1.87</sub>	2.33 <sup>8.79</sup> <sub>–0.86</sub>	0.28 <sup>0.02</sup> <sub>–0.02</sub>	0.55 <sup>0.02</sup> <sub>–0.01</sub>
IRAS08311–2459	664.2 <sup>74.29</sup> <sub>–37.32</sub>	31.8 <sup>4.63</sup> <sub>–13.73</sub>	17.2 <sup>1.5</sup> <sub>–0.85</sub>	33.47 <sup>4.69</sup> <sub>–13.63</sub>	0.34 <sup>0.09</sup> <sub>–0.06</sub>	1.79 <sup>0.54</sup> <sub>–0.25</sub>
IRAS08572+3915	155.5 <sup>18.02</sup> <sub>–48.19</sub>	2.19 <sup>0.19</sup> <sub>–0.15</sub>	0.9 <sup>0.14</sup> <sub>–0.07</sub>	2.28 <sup>0.22</sup> <sub>–0.16</sub>	0.96 <sup>0.01</sup> <sub>–0.01</sub>	14.2 <sup>1.38</sup> <sub>–1.29</sub>
IRAS09022–3615	471.9 <sup>12.67</sup> <sub>–21.17</sub>	12.93 <sup>2.89</sup> <sub>–1.95</sub>	13.12 <sup>0.8</sup> <sub>–0.81</sub>	14.3 <sup>2.8</sup> <sub>–1.94</sub>	0.15 <sup>0.06</sup> <sub>–0.03</sub>	1.53 <sup>0.34</sup> <sub>–0.16</sub>
IRAS10378+1109	436.9 <sup>25.77</sup> <sub>–40.16</sub>	11.46 <sup>0.71</sup> <sub>–1.38</sub>	11.62 <sup>0.61</sup> <sub>–1.06</sub>	12.68 <sup>0.66</sup> <sub>–1.47</sub>	0.64 <sup>0.11</sup> <sub>–0.09</sub>	6.07 <sup>1.94</sup> <sub>–0.5</sub>
IRAS10565+2448	395.6 <sup>13.45</sup> <sub>–13.02</sub>	9.94 <sup>0.7</sup> <sub>–0.51</sub>	12.13 <sup>0.39</sup> <sub>–0.48</sub>	11.13 <sup>0.67</sup> <sub>–0.5</sub>	0.27 <sup>0.01</sup> <sub>–0.02</sub>	3.31 <sup>0.09</sup> <sub>–0.26</sub>
IRAS11095–0238	188.3 <sup>26.93</sup> <sub>–18.01</sub>	2.5 <sup>1.28</sup> <sub>–0.82</sub>	3.83 <sup>1.23</sup> <sub>–1.64</sub>	2.79 <sup>1.38</sup> <sub>–0.64</sub>	0.88 <sup>0.06</sup> <sub>–0.02</sub>	8.1 <sup>3.3</sup> <sub>–0.79</sub>
IRAS12071–0444	365.7 <sup>44.46</sup> <sub>–36.9</sub>	17.75 <sup>0.7</sup> <sub>–3.39</sub>	2.17 <sup>1.0</sup> <sub>–0.21</sub>	17.97 <sup>0.68</sup> <sub>–3.37</sub>	0.61 <sup>0.07</sup> <sub>–0.01</sub>	2.82 <sup>0.39</sup> <sub>–0.16</sub>
IRAS13120–5453	659.2 <sup>40.75</sup> <sub>–44.06</sub>	6.68 <sup>2.93</sup> <sub>–2.56</sub>	19.86 <sup>1.14</sup> <sub>–2.21</sub>	8.74 <sup>2.9</sup> <sub>–2.85</sub>	0.09 <sup>0.02</sup> <sub>–0.01</sub>	2.1 <sup>0.19</sup> <sub>–0.13</sub>
IRAS13451+1232	143.8 <sup>20.13</sup> <sub>–27.22</sub>	25.61 <sup>11.43</sup> <sub>–3.77</sub>	1.8 <sup>0.1</sup> <sub>–0.34</sub>	25.8 <sup>11.38</sup> <sub>–3.76</sub>	0.82 <sup>0.05</sup> <sub>–0.01</sub>	3.65 <sup>0.71</sup> <sub>–0.11</sub>
IRAS14348–1447	514.3 <sup>50.25</sup> <sub>–29.42</sub>	13.48 <sup>8.48</sup> <sub>–3.64</sub>	15.4 <sup>1.18</sup> <sub>–0.82</sub>	14.98 <sup>8.51</sup> <sub>–3.61</sub>	0.19 <sup>0.07</sup> <sub>–0.04</sub>	3.73 <sup>1.3</sup> <sub>–0.47</sub>
IRAS14378–3651	289.2 <sup>35.42</sup> <sub>–22.87</sub>	8.1 <sup>0.77</sup> <sub>–1.64</sub>	8.91 <sup>1.01</sup> <sub>–0.75</sub>	8.95 <sup>0.76</sup> <sub>–1.44</sub>	0.31 <sup>0.02</sup> <sub>–0.06</sub>	3.6 <sup>0.23</sup> <sub>–0.68</sub>
IRAS15250+3609	147.5 <sup>9.02</sup> <sub>–9.49</sub>	2.32 <sup>0.1</sup> <sub>–0.11</sub>	3.81 <sup>0.45</sup> <sub>–0.49</sub>	2.68 <sup>0.11</sup> <sub>–0.09</sub>	0.81 <sup>0.03</sup> <sub>–0.03</sub>	6.9 <sup>0.65</sup> <sub>–0.53</sub>
IRAS15462–0450	269.0 <sup>10.0</sup> <sub>–17.79</sub>	8.54 <sup>1.96</sup> <sub>–4.37</sub>	4.4 <sup>1.09</sup> <sub>–1.18</sub>	9.03 <sup>2.08</sup> <sub>–4.38</sub>	0.34 <sup>0.06</sup> <sub>–0.06</sub>	1.73 <sup>0.46</sup> <sub>–0.46</sub>
IRAS16090–0139	783.4 <sup>77.66</sup> <sub>–45.3</sub>	8.84 <sup>8.21</sup> <sub>–3.58</sub>	23.86 <sup>2.13</sup> <sub>–1.45</sub>	11.21 <sup>8.18</sup> <sub>–3.64</sub>	0.21 <sup>0.04</sup> <sub>–0.04</sub>	2.73 <sup>0.5</sup> <sub>–0.31</sub>
IRAS17208–0014	809.6 <sup>69.15</sup> <sub>–30.6</sub>	6.31 <sup>0.03</sup> <sub>–2.71</sub>	24.22 <sup>2.55</sup> <sub>–0.47</sub>	8.72 <sup>0.01</sup> <sub>–2.44</sub>	0.05 <sup>0.0</sup> <sub>–0.01</sub>	2.52 <sup>0.27</sup> <sub>–0.37</sub>
IRAS19254–7245	121.0 <sup>6.34</sup> <sub>–15.08</sub>	51.24 <sup>12.16</sup> <sub>–7.97</sub>	1.25 <sup>0.14</sup> <sub>–0.13</sub>	51.38 <sup>12.17</sup> <sub>–7.98</sub>	0.71 <sup>0.07</sup> <sub>–0.05</sub>	3.91 <sup>0.55</sup> <sub>–0.36</sub>
IRAS19297–0406	660.0 <sup>113.5</sup> <sub>–21.24</sub>	20.25 <sup>1.96</sup> <sub>–2.62</sub>	20.3 <sup>2.95</sup> <sub>–0.89</sub>	22.26 <sup>2.04</sup> <sub>–2.58</sub>	0.12 <sup>0.05</sup> <sub>–0.03</sub>	2.0 <sup>0.56</sup> <sub>–0.28</sub>
IRAS20087–0308	1108.0 <sup>33.56</sup> <sub>–58.6</sub>	15.61 <sup>2.0</sup> <sub>–2.17</sub>	33.77 <sup>1.05</sup> <sub>–1.85</sub>	18.99 <sup>2.13</sup> <sub>–2.11</sub>	0.12 <sup>0.02</sup> <sub>–0.02</sub>	3.51 <sup>0.36</sup> <sub>–0.34</sub>
IRAS20100–4156	768.0 <sup>42.35</sup> <sub>–50.45</sub>	10.47 <sup>2.3</sup> <sub>–1.39</sub>	12.98 <sup>3.04</sup> <sub>–4.55</sub>	11.95 <sup>2.12</sup> <sub>–1.66</sub>	0.28 <sup>0.03</sup> <sub>–0.02</sub>	3.16 <sup>0.41</sup> <sub>–0.24</sub>
IRAS20414–1651	495.6 <sup>71.76</sup> <sub>–4.92</sub>	5.25 <sup>0.15</sup> <sub>–1.7</sub>	15.02 <sup>1.83</sup> <sub>–0.06</sub>	6.74 <sup>0.34</sup> <sub>–1.69</sub>	0.15 <sup>0.07</sup> <sub>–0.03</sub>	4.46 <sup>2.07</sup> <sub>–0.7</sub>
IRAS20551–4250	168.1 <sup>20.4</sup> <sub>–10.63</sub>	4.31 <sup>0.23</sup> <sub>–0.16</sub>	2.07 <sup>0.66</sup> <sub>–0.49</sub>	4.55 <sup>0.15</sup> <sub>–0.14</sub>	0.55 <sup>0.03</sup> <sub>–0.06</sub>	3.84 <sup>0.45</sup> <sub>–0.38</sub>
IRAS22491–1808	215.7 <sup>21.48</sup> <sub>–46.05</sub>	4.98 <sup>0.14</sup> <sub>–0.99</sub>	2.59 <sup>4.17</sup> <sub>–0.83</sub>	5.21 <sup>0.14</sup> <sub>–0.51</sub>	0.56 <sup>0.15</sup> <sub>–0.06</sub>	5.01 <sup>1.68</sup> <sub>–0.42</sub>
IRAS23128–5919	192.8 <sup>9.28</sup> <sub>–17.54</sub>	4.84 <sup>0.29</sup> <sub>–0.21</sub>	2.54 <sup>0.69</sup> <sub>–0.84</sub>	5.16 <sup>0.19</sup> <sub>–0.18</sub>	0.29 <sup>0.02</sup> <sub>–0.04</sub>	2.14 <sup>0.14</sup> <sub>–0.16</sub>
IRAS23230–6926	308.5 <sup>11.22</sup> <sub>–14.01</sub>	6.9 <sup>0.53</sup> <sub>–0.45</sub>	3.72 <sup>1.0</sup> <sub>–0.76</sub>	7.28 <sup>0.54</sup> <sub>–0.44</sub>	0.51 <sup>0.04</sup> <sub>–0.04</sub>	4.08 <sup>0.39</sup> <sub>–0.4</sub>
IRAS23253–5415	674.9 <sup>52.35</sup> <sub>–79.95</sub>	27.38 <sup>1.65</sup> <sub>–8.61</sub>	19.42 <sup>0.95</sup> <sub>–2.51</sub>	29.73 <sup>1.41</sup> <sub>–9.01</sub>	0.37 <sup>0.04</sup> <sub>–0.02</sub>	4.22 <sup>0.43</sup> <sub>–0.29</sub>
IRAS23365+3604	288.3 <sup>99.23</sup> <sub>–22.81</sub>	11.77 <sup>0.71</sup> <sub>–2.34</sub>	6.68 <sup>1.97</sup> <sub>–1.61</sub>	12.27 <sup>1.0</sup> <sub>–2.18</sub>	0.72 <sup>0.02</sup> <sub>–0.06</sub>	7.42 <sup>2.17</sup> <sub>–1.36</sub>
Mrk1014	787.1 <sup>49.55</sup> <sub>–58.96</sub>	0.01 <sup>14.36</sup> <sub>–0.01</sub>	15.0 <sup>1.76</sup> <sub>–2.19</sub>	1.87 <sup>13.85</sup> <sub>–0.39</sub>	0.16 <sup>0.0</sup> <sub>–0.01</sub>	0.6 <sup>0.01</sup> <sub>–0.03</sub>
UGC5101	169.8 <sup>9.08</sup> <sub>–8.86</sub>	20.14 <sup>1.26</sup> <sub>–0.77</sub>	1.66 <sup>0.14</sup> <sub>–0.15</sub>	20.32 <sup>1.24</sup> <sub>–0.78</sub>	0.22 <sup>0.03</sup> <sub>–0.02</sub>	2.42 <sup>0.24</sup> <sub>–0.15</sub>
Mrk231	524.3 <sup>35.12</sup> <sub>–36.04</sub>	12.39 <sup>3.3</sup> <sub>–0.74</sub>	10.03 <sup>1.92</sup> <sub>–2.49</sub>	13.32 <sup>3.4</sup> <sub>–0.86</sub>	0.64 <sup>0.02</sup> <sub>–0.06</sub>	2.44 <sup>0.2</sup> <sub>–0.34</sub>
Mrk273	356.3 <sup>17.61</sup> <sub>–13.92</sub>	11.77 <sup>0.66</sup> <sub>–0.47</sub>	9.6 <sup>0.75</sup> <sub>–0.71</sub>	12.7 <sup>0.65</sup> <sub>–0.42</sub>	0.19 <sup>0.08</sup> <sub>–0.03</sub>	2.68 <sup>0.73</sup> <sub>–0.35</sub>
Mrk463	40.28 <sup>6.02</sup> <sub>–5.33</sub>	14.9 <sup>0.82</sup> <sub>–0.82</sub>	0.62 <sup>0.31</sup> <sub>–0.22</sub>	14.99 <sup>0.78</sup> <sub>–0.85</sub>	0.82 <sup>0.03</sup> <sub>–0.03</sub>	1.97 <sup>0.05</sup> <sub>–0.57</sub>
Arp220	216.8 <sup>4.28</sup> <sub>–12.76</sub>	8.71 <sup>0.12</sup> <sub>–0.27</sub>	5.66 <sup>0.2</sup> <sub>–0.3</sub>	9.24 <sup>0.16</sup> <sub>–0.24</sub>	0.82 <sup>0.01</sup> <sub>–0.03</sub>	8.53 <sup>0.52</sup> <sub>–0.28</sub>
NGC6240	163.6 <sup>19.99</sup> <sub>–21.91</sub>	10.08 <sup>0.96</sup> <sub>–1.11</sub>	4.84 <sup>0.44</sup> <sub>–1.06</sub>	10.52 <sup>0.97</sup> <sub>–1.12</sub>	0.54 <sup>0.06</sup> <sub>–0.1</sub>	5.73 <sup>0.84</sup> <sub>–0.78</sub>

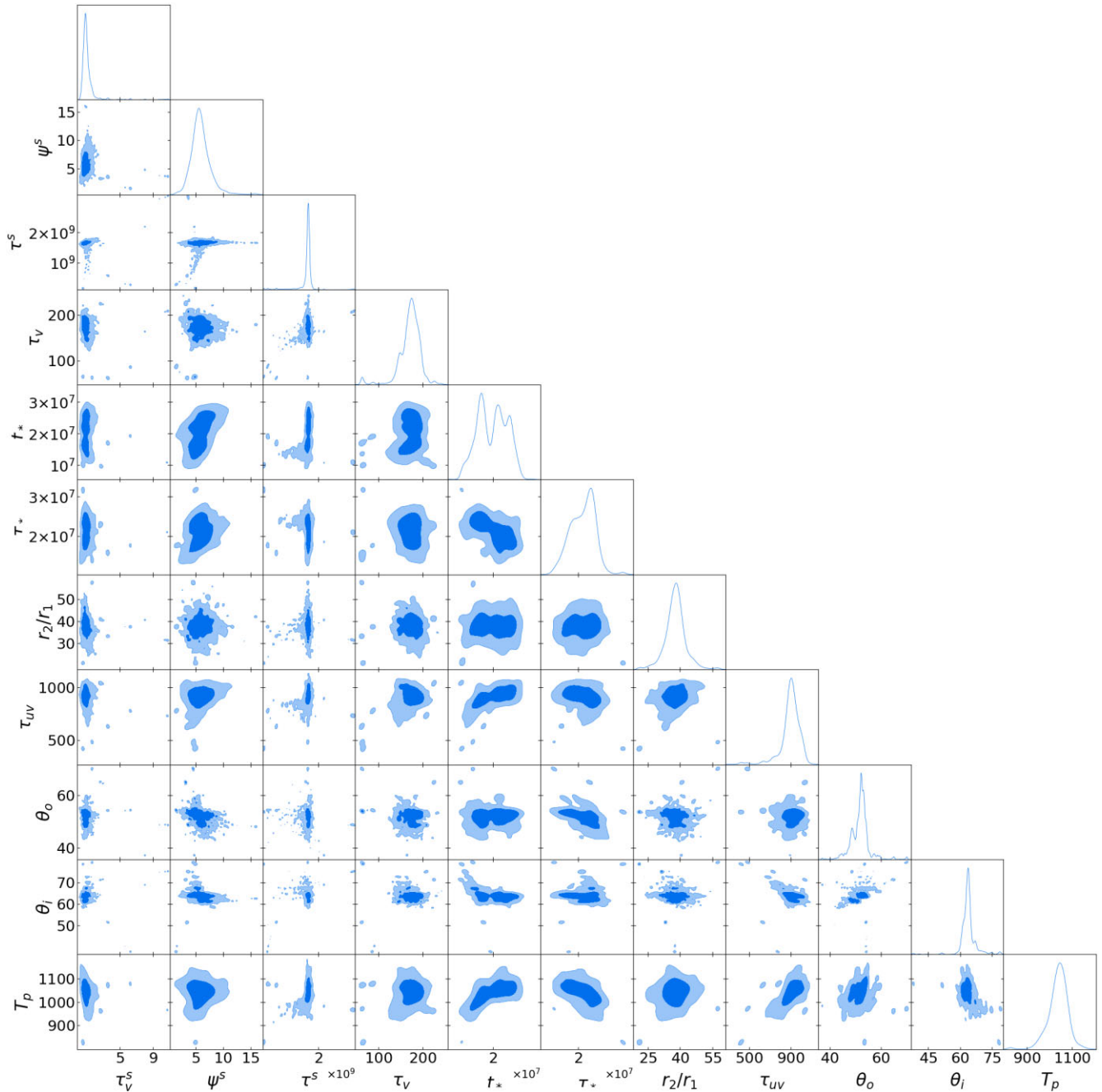


**Figure 4.** Corner plot of the ULIRG IRAS 05189–2524, which shows that most of the parameters of the models are constrained very well with very little degeneracy.

It was found in particular by Young et al. (1996) to show broad lines in polarized flux. NGC 1068 was also the first LIRG that was recognized to have polar dust (Braatz et al. 1993; Cameron et al. 1993; Efstathiou et al. 1995). Efstathiou et al. (2022) found that a fit with polar dust provides a better fit to the SED of IRAS 05189–2524 compared to a fit without polar dust. Reynolds et al. (2022) found evidence that IRAS 05189–2524 recently experienced a dust obscured tidal disruption event (TDE) with an IR echo from polar dust. This phenomenon was first proposed for the TDE in the LIRG Arp 299 by Mattila et al. (2018).

We find that a fit with SMART with an obscured AGN and polar dust provides a good fit to the SED. The model for polar dust incorporated in SMART has the temperature of polar dust as a

free parameter, whereas Efstathiou et al. (2022) considered only a single temperature for the polar dust. We find that the polar dust in IRAS 05189–2524 has a temperature of  $1050.6^{+28.7}_{-23.2}$  K. In Tables A1, A2, 3, and 4 we list all of the important fitted parameters and extracted physical properties for this ULIRG. The SED fit plot is shown in Fig. A1.

#### 4.2 Fit of a ULIRG with an unobscured quasar and also associated with polar dust

The galaxy IRAS 07598+6508 is the only ULIRG in the HERUS sample (apart from 3C 273 which we do not fit, as it clearly has a strong contribution in the submillimetre from radio emission), which

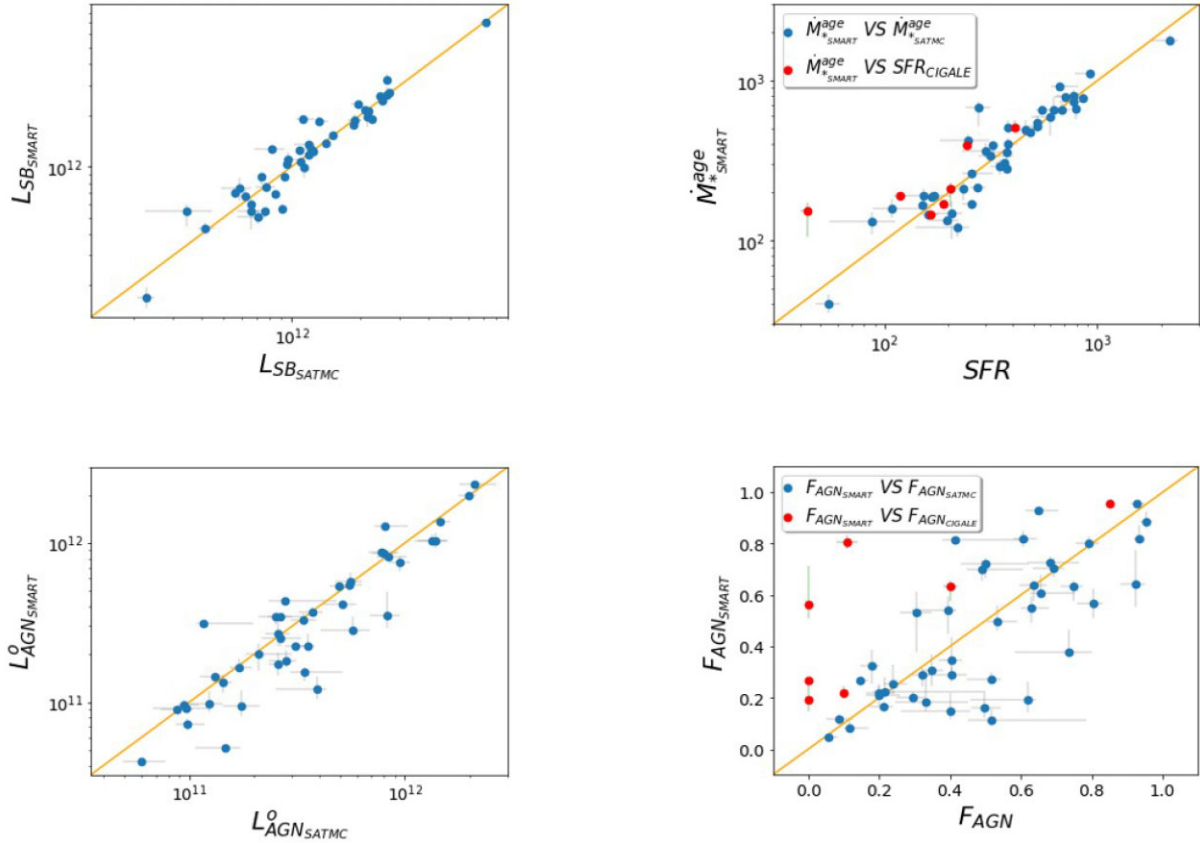


**Figure 5.** Plot of representative physical quantities for the 42 HERUS local ULIRGs extracted by SMART against the same quantities extracted by Efstathiou et al. (2022) using SATMC (blue). In two of the panels we also plot with red the corresponding quantities extracted by CIGALE for seven of the HERUS ULIRGs by Paspaliaris et al. (2021). *Top left:* Starburst luminosity. *Top right:* SFR. *Bottom left:* Observed AGN torus luminosity. *Bottom right:* AGN fraction.

shows clear signs of a type 1 AGN with a strong optical continuum with a power-law shape. This ULIRG was therefore fitted with a type 1 AGN by Efstathiou et al. (2022).

In Fig. 6 we fit IRAS 07598+6508 with all four combinations of models without polar dust. We observe that in all cases there is evidence that the torus model by itself can not reproduce the (near-infrared) NIR spectrum. We attribute this to the presence of polar dust in this object, which is more visible because of the assumed face-on inclination. We can also see this from the reduced  $\chi^2$  we provide in Table 5. The  $\chi^2_{\min,v}$  of the CYGNUS fit without polar dust is much higher compared to the fit with polar dust shown in Table A1. The important fitted parameters and extracted physical properties for this ULIRG are listed in Tables A1, A2, 3, and 4. The SED fit plot with polar dust is shown in Fig. A2.

#### 4.3 Fit of the deeply obscured ULIRG IRAS 08572+3915

Efstathiou et al. (2014) proposed that the ULIRG IRAS 08572+3915 is the most luminous IR galaxy in the local ( $z < 0.2$ ) Universe. It is an example of an interacting ULIRG, which exhibits one of the deepest silicate absorption features observed in a galaxy. Efstathiou et al. (2014) proposed that the deep silicate absorption feature is due to the fact that the AGN torus in this object is observed almost edge-on. The huge luminosity of this object, which approaches or exceeds  $10^{13} L_{\odot}$ , is due to the large anisotropy correction.

To explore further the properties of this system, we fit the SED with all four combinations of AGN radiative transfer models. Two of the combinations assume a smooth torus geometry (Efstathiou & Rowan-Robinson 1995; Fritz et al. 2006) and two combinations assume a two-phase geometry (Siebenmorgen et al. 2015; Stalevski et al. 2016).

It is interesting that the smooth models fit much better than the two-phase models. The last two in particular do not fit the deep silicate absorption feature of this galaxy and predict that the object is starburst-dominated. According to the fits of the smooth models, which perform much better, this is an AGN-dominated object. In Tables 6, A3, and A4 we list all of the important fitted parameters and extracted physical properties of the four combinations of models. The comparison SED fit plots are shown in Fig. 7. The CYGNUS combination of models gives a  $\chi^2_{\min,v}$  equal to 1.67, which is significantly lower than the  $\chi^2_{\min,v}$  given by the other three combinations and shows that the CYGNUS AGN model fits much better than the other models. The Fritz et al. (2006) AGN model gives  $\chi^2_{\min,v} = 4.1$ , the SKIRTOR AGN model gives  $\chi^2_{\min,v} = 8.2$  and the AGN model of Siebenmorgen et al. (2015) gives  $\chi^2_{\min,v} = 8.28$ .

#### 4.4 Fit of a LIRG associated with a spiral galaxy

To explore the option of fitting with a disc as a host galaxy component, we fitted the LIRG VV 340a, which belongs to a pair of spiral galaxies known as Arp 302, with the northern galaxy, VV 340a, being viewed

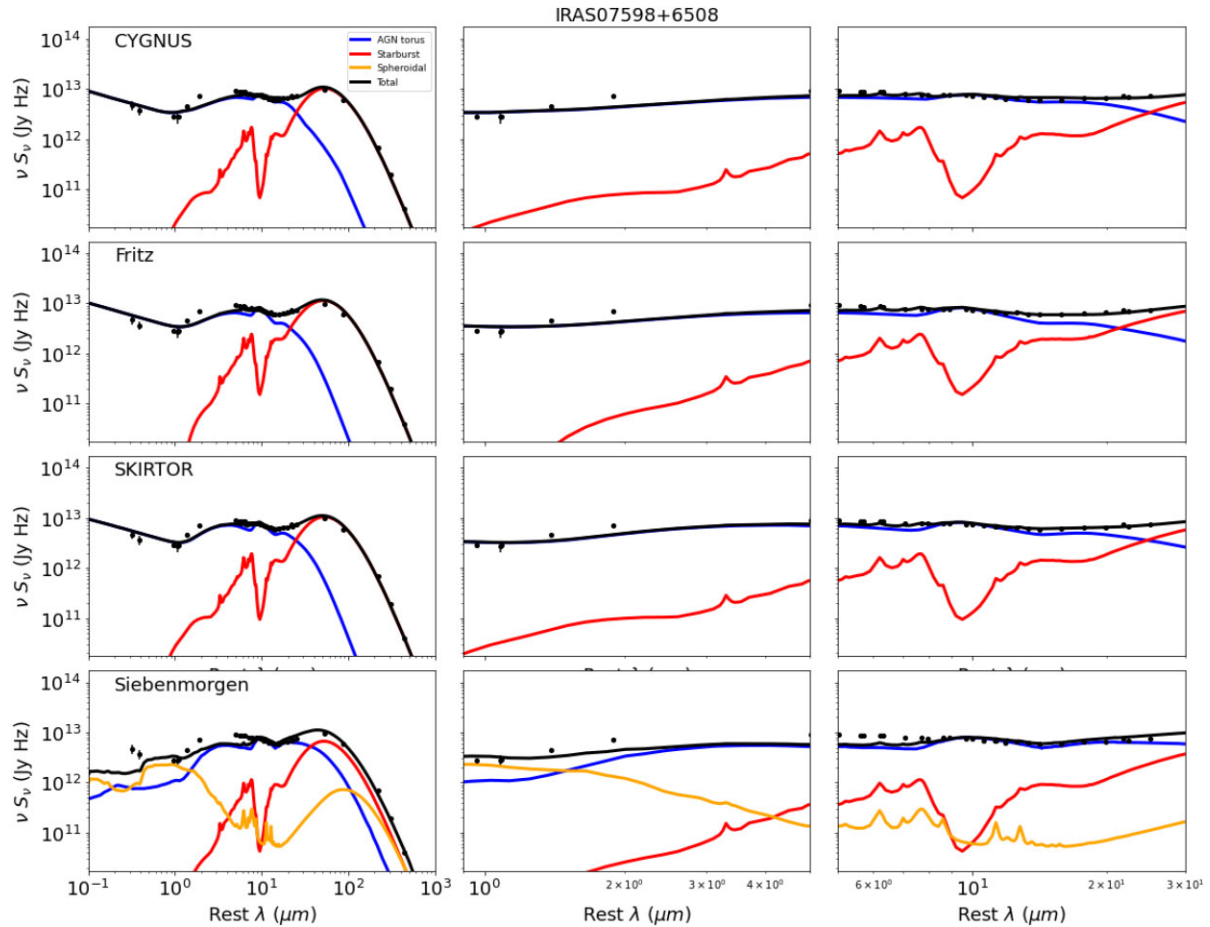


**Figure 6.** Comparison SED fit plots of IRAS 07598+6508 without using the polar dust component. The AGN torus, starburst, spheroidal host and total emission are plotted as shown in the legend. The top row shows fits with the CYGNUS combination of models. The second row shows fits with the CYGNUS AGN model replaced by the Fritz et al. (2006) model, the third row replaces the CYGNUS AGN model with the SKIRTOR model, while the bottom row replaces the CYGNUS AGN model with the Siebenmorgen et al. (2015) model. The left panel shows the fit over 0.1–1000  $\mu\text{m}$  range, the middle panel the approximate range of the NIRspec instrument on *JWST* and the right panel the corresponding range of the MIRI instrument.

**Table 5.** Reduced  $\chi^2$  of fits for IRAS 07598+6508 with all combinations of models without using the polar dust component.

AGN model	$\chi^2_{\text{min},\nu}$
CYGNUS	0.71
Fritz et al. (2006)	0.89
SKIRTOR	0.66
Siebenmorgen et al. (2015)	2.82

edge-on and the southern galaxy, VV 340b, viewed face-on. This pair of galaxies was discussed extensively by Armus et al. (2009). We fitted this object twice, using the two different host galaxy models that we have available, the spheroidal and the disc model.

We observe that the disc model appears to fit better not just the photometry but also the *Spitzer* spectroscopy. The difference in the  $\chi^2_{\text{min},\nu}$  of the two different fits is also significant, with the disc model providing the minimum value of 2.84, while the spheroidal model provides a  $\chi^2_{\text{min},\nu}$  of 5.65, a factor of two higher. The best fits with the two different host geometries are listed in Tables 7, A5, and A6 and plotted in Fig. 8. The predicted disc morphology is consistent with the nature of this galaxy. It is very interesting that the fit of VV 340a predicts an almost edge-on view and this agrees with the

image of the galaxy. This example is an indication that SMART may be a useful tool for galaxy morphological classification, especially in cases where an image of the galaxy is not available.

Jiang et al. (2024) presented *XMM-Newton* data of VV 340a and VV 340b from which they find evidence of a heavily obscured Seyfert 2-like AGN in VV 340a. This is in agreement with our fit, which predicts the presence of an obscured AGN with an anisotropy-corrected AGN luminosity of  $0.25^{+0.06}_{-0.04} \times 10^{12} L_{\odot}$ . Our model, however, predicts a much higher SFR compared with the estimate of Jiang et al. (2024) of  $1\text{--}2 M_{\odot} \text{ yr}^{-1}$  for this galaxy, which is based entirely on X-ray data.

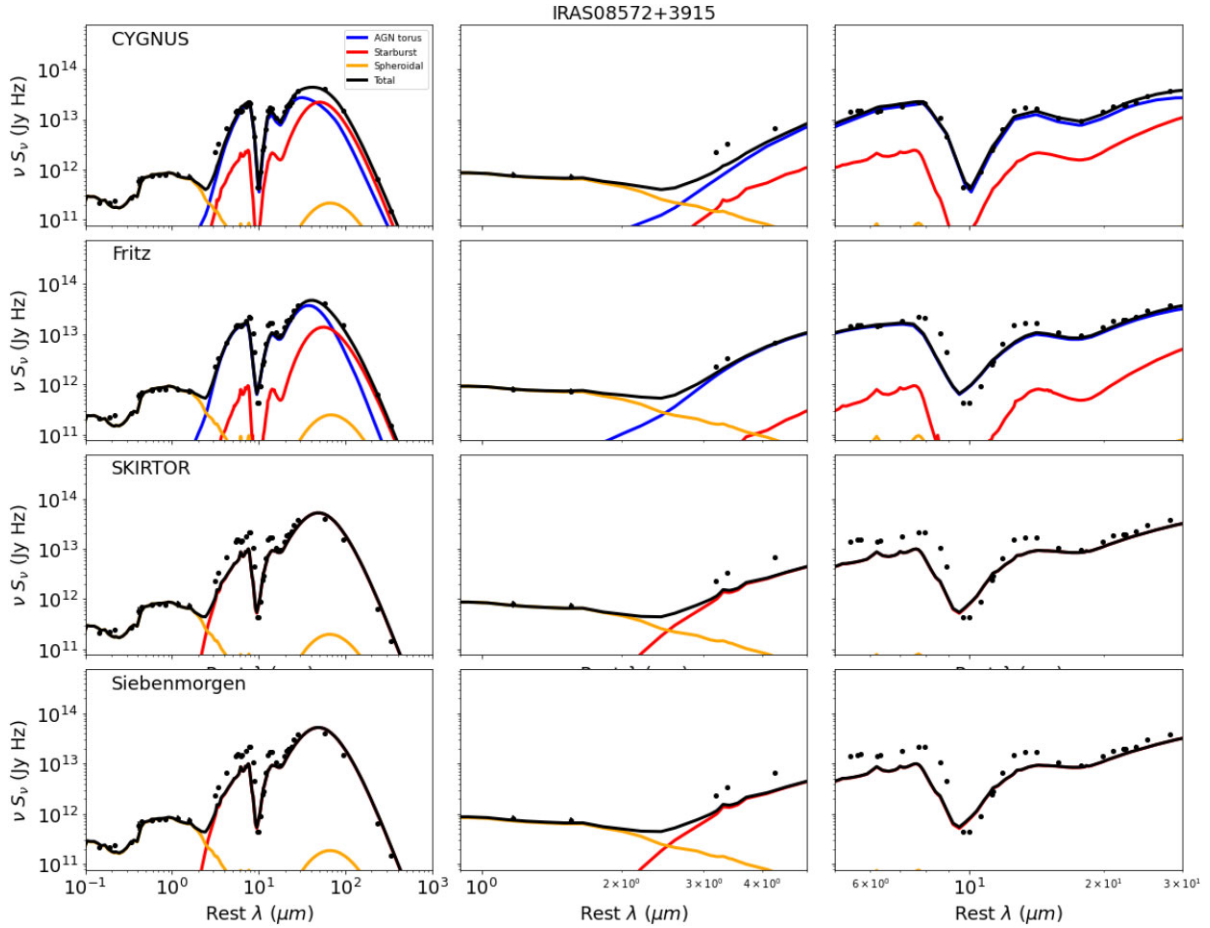
#### 4.5 Fit of a hyperluminous obscured quasar at $z \sim 4.3$

The HLIRG HELP J100156.75+022344.7 at a photometric redshift of  $z \sim 4.3$  was discovered in the Cosmological Evolution Survey (COSMOS) field, one of the fields studied by HELP. This is one of only a few  $z > 4$  hyperluminous obscured quasars discovered to date and, according to the CYGNUS model presented by Efstathiou et al. (2021), it is AGN-dominated with an AGN fraction of 82 percent. Efstathiou et al. (2021) also fitted HELP J100156.75+022344.7 with CIGALE and arrived at a similar conclusion. HELP J100156.75+022344.7 is predicted to have an



**Table 6.** Selected fitted parameters for IRAS 08572+3915.

AGN model	$t_*$ ( $10^7$ yr)	$\tau_*$ ( $10^7$ yr)					$\theta_i$ ( $^\circ$ )
CYGNUS			$r_2/r_1$	$\tau_{uv}$	$\theta_o$ ( $^\circ$ )		
	$0.64^{0.28}_{-0.1}$	$1.79^{0.34}_{-0.25}$	$58.5^{9.8}_{-8.38}$	$612.99^{14.44}_{-21.13}$	$72.66^{1.05}_{-0.89}$		$79.04^{0.74}_{-0.65}$
Fritz et al. (2006)			$r_2/r_1$	$\tau_{9.7 \mu\text{m}}$	$\theta_o$ ( $^\circ$ )		
	$2.37^{0.6}_{-0.6}$	$1.93^{0.17}_{-0.17}$	$117.4^{18.11}_{-18.11}$	$9.39^{0.03}_{-0.03}$	$54.48^{0.61}_{-0.61}$		$84.54^{0.01}_{-0.01}$
SKIRTOR			$r_2/r_1$	$\tau_{9.7 \mu\text{m}}$	$\theta_o$ ( $^\circ$ )		
	$0.51^{0.02}_{-0.01}$	$1.89^{0.53}_{-0.22}$	$23.96^{4.5}_{-4.72}$	$5.67^{2.13}_{-0.7}$	$47.31^{16.22}_{-11.34}$		$60.72^{13.35}_{-13.6}$
Siebenmorgen et al. (2015)			$A_c$	$V_c$	$A_d$		
	$0.51^{0.02}_{-0.01}$	$2.05^{0.74}_{-0.25}$	$8.36^{14.42}_{-6.23}$	$57.98^{47.19}_{-21.28}$	$211.06^{126.38}_{-58.5}$		$86.88^{6.87}_{-2.63}$

**Figure 7.** Comparison SED fit plots of IRAS 08572+3915. The AGN torus, starburst, spheroidal host and total emission are plotted as shown in the legend. The top row shows fits with the CYGNUS combination of models. The second row shows fits with the CYGNUS AGN model replaced by the Fritz et al. (2006) model, the third row replaces the CYGNUS AGN model with the SKIRTOR model, while the bottom row replaces the CYGNUS AGN model with the Siebenmorgen et al. (2015) model. The left panel shows the fit over 0.1–1000  $\mu\text{m}$  range, the middle panel the approximate range of the NIRSpec instrument on *JWST* and the right panel the corresponding range of the MIRI instrument.**Table 7.** Selected fitted parameters for VV 340a.

Host galaxy model	$t_*$ ( $10^7$ yr)	$\tau_*$ ( $10^7$ yr)	$r_2/r_1$	$\tau_{uv}$	$\theta_o$ ( $^\circ$ )	$\theta_i$ ( $^\circ$ )
Spheroidal	$3.38^{0.02}_{-0.16}$	$1.46^{0.26}_{-0.22}$	$78.02^{4.58}_{-6.31}$	$760.03^{342.98}_{-182.2}$	$56.9^{3.32}_{-3.09}$	$55.81^{3.95}_{-4.56}$
Disc	$1.09^{0.1}_{-0.07}$	$2.02^{0.05}_{-0.09}$	$89.72^{5.24}_{-5.15}$	$863.0^{117.51}_{-51.98}$	$66.53^{1.41}_{-1.56}$	$74.07^{0.53}_{-0.66}$

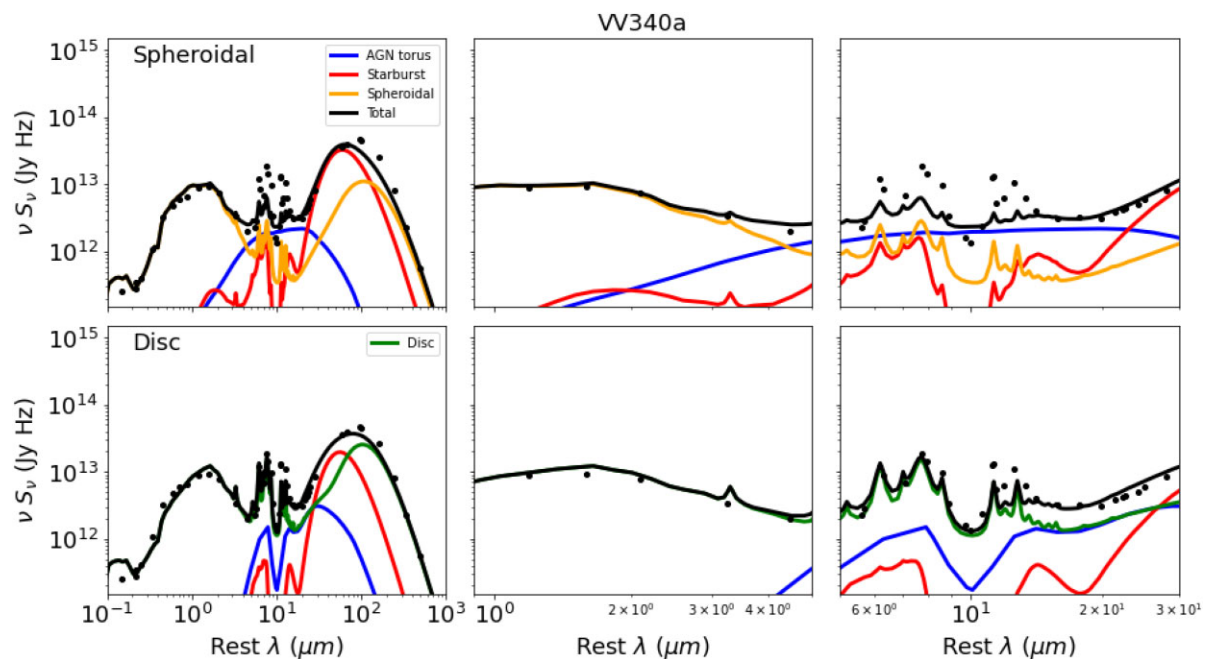


**Figure 8.** Comparison SED fit plots of VV 340a, which is a LIRG associated with a spiral galaxy. The AGN torus, starburst, host and total emission are plotted as shown in the legend. The top row shows the fit with the spheroidal host galaxy model, while the second row replaces the spheroidal host galaxy model with the disc host galaxy model. The left panel shows the fit over  $0.1 - 1000 \mu\text{m}$  range, the middle panel the approximate range of the NIRSpec instrument on *JWST* and the right panel the corresponding range of the MIRI instrument.

SFR of  $1051_{-268}^{+109} \text{ M}_{\odot} \text{ yr}^{-1}$  according to CYGNUS and  $991_{-223}^{+223} \text{ M}_{\odot} \text{ yr}^{-1}$  according to CIGALE.

In this paper we fit HELP.J100156.75+022344.7 with the four different combinations of models, in order to quantify the uncertainty in the AGN fraction and SFR. As noted by Efstathiou et al. (2021), in the SUPRIME N921 filter we see an excess in the photometry that deviates significantly from the fit. This could be due to an emission line or a problem in the data reduction. As in the models we use in our method emission lines are not included, we opted to omit this data point from the fit.

For all the fits we fixed  $\tau_* = 2 \times 10^7 \text{ yr}$  and two other parameters. For the fits with the CYGNUS and Fritz et al. (2006) AGN models we additionally fixed  $\theta_o = 45^\circ$  and  $r_2/r_1 = 60$ . For the fit with the AGN model SKIRTOR we fixed  $\theta_o = 45^\circ$  and  $r_2/r_1 = 20$ , whereas for the fit with the Siebenmorgen et al. (2015) AGN model we fixed  $A_c = 3$  and  $V_c = 40$ . The best fits with all combinations of models are listed in Tables 8, A7, and A8, and plotted in Fig. 9. The CYGNUS, Fritz et al. (2006) and SKIRTOR models predict a similar solution for the AGN fraction and SFR, although there are significant differences in the  $\chi^2_{\text{min},v}$ , with the CYGNUS model giving the minimum value of 6.09. The SKIRTOR model gives  $\chi^2_{\text{min},v} = 6.69$  and the Fritz et al. (2006) model gives  $\chi^2_{\text{min},v} = 8.67$ . The model of Siebenmorgen et al. (2015) gives the worst fit with  $\chi^2_{\text{min},v} = 12.03$  and predicts a significantly lower SFR compared with the other models.

## 5 CONCLUSIONS

(i) In this paper we present SMART, a new fast code of fitting SEDs exclusively with radiative transfer models. The method employs the MCMC code *emcee* and uses pre-computed libraries for starbursts, AGN tori, and host galaxies, which can be modelled either with a spheroidal or disc geometry. The code takes comparable time to energy balance codes like CIGALE and MAGPHYS. The

method is flexible in that it can fit SEDs which include MIR spectrophotometry, but also galaxies where more limited photometry is available.

(ii) As SMART can fit an SED with four different AGN torus models, it allows us to constrain the properties of the obscuring torus in AGN and quantify the uncertainties in AGN fraction and SFR. We consider four different AGN torus models: the smooth tapered discs of Efstathiou & Rowan-Robinson (1995), the smooth flared discs of Fritz et al. (2006), the two-phase flared discs of Stalevski et al. (2012, 2016) and the two phase model of Siebenmorgen et al. (2015). The first three models assume a normal interstellar mixture, whereas the model of Siebenmorgen et al. (2015) assumes fluffy grains, which are more efficient at emitting at submillimetre wavelengths.

(iii) We test the method with the HERUS sample of ULIRGs and compare our results with those obtained with the SATMC code by Efstathiou et al. (2022) and by Paspaliaris et al. (2021) using CIGALE. We find that the results obtained with SMART agree very well with those obtained with SATMC, except for the AGN fraction, which shows considerable scatter. We attribute this to the strong dependence of this quantity on the inclination. The SFRs predicted by CIGALE generally agree with those with SMART, but the AGN fraction is significantly lower, partly because CIGALE does not apply any anisotropy corrections to the AGN luminosity.

(iv) SMART is developed in PYTHON and is available at <https://github.com/ch-var/SMART.git>.

We also briefly discuss some ideas for future development of SMART:

(i) The main limitation of SMART is that it currently assumes constant metallicity and a parametric SFH and in particular a delayed exponential for the host galaxy and an exponential for the starburst. Future developments of the code will allow treatment of non-parametric SFH and metallicity histories.

**Table 8.** Selected fitted parameters for HELP J100156.75+022344.7.

AGN model	$\tau_v$	$t_*$ ( $10^7$ yr)	$\theta_i$ ( $^\circ$ )
CYGNUS	$125.81^{34.15}_{-17.31}$	$2.02^{0.19}_{-0.71}$	$55.18^{0.48}_{-1.8}$
Fritz et al. (2006)	$107.94^{33.15}_{-30.26}$	$1.6^{0.45}_{-0.44}$	$79.08^{4.53}_{-4.11}$
SKIRTOR	$114.31^{92.24}_{-41.79}$	$1.82^{1.05}_{-0.79}$	$64.79^{5.57}_{-12.75}$
Siebenmorgen et al. (2015)	$133.18^{54.28}_{-45.45}$	$1.53^{0.82}_{-0.76}$	$60.1^{5.86}_{-6.16}$

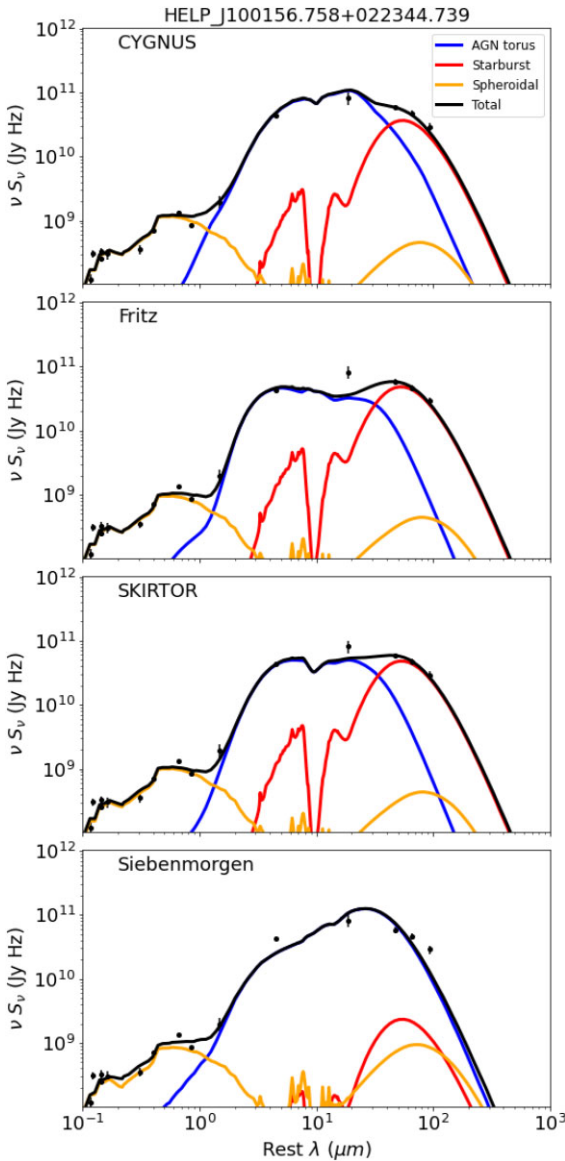


**Figure 9.** Comparison SED fit plots of the hyperluminous galaxy HELP J100156.75+022344.7 at a photometric redshift of  $z \sim 4.3$ . The AGN torus, starburst, spheroidal host and total emission are plotted as shown in the legend. The top row shows fits with the CYGNUS combination of models. The second row shows fits with the CYGNUS AGN model replaced by the Fritz et al. (2006) model, the third row replaces the CYGNUS AGN model with the SKIRTOR model, while the bottom row replaces the CYGNUS AGN model with the Siebenmorgen et al. (2015) model.

(ii) Another limitation of SMART is that it does not model nebular lines. A future development could be to add nebular emission in the libraries used by SMART. To do this, we would need to increase the spectral resolution of the models, which is currently 223 points, to cover the wavelength range from the UV to the millimetre.

(iii) SMART currently fits the UV to millimetre SEDs. Therefore, another limitation is that it does not model X-ray emission. This could be an additional extension of SMART. We could follow the same methodology adopted in other codes, such as X-CIGALE (Yang et al. 2020).

We conclude that SMART promises to be very useful for understanding galaxies and AGN at any redshift in the JWST era, as well as galaxy formation and evolution more generally.

## ACKNOWLEDGEMENTS

We would like to thank the anonymous referee for useful comments and suggestions. The authors acknowledge support from the projects CYGNUS (contract number 4000126896) and CYGNUS+ (contract number 4000139319) funded by the European Space Agency. CV acknowledges a Ph.D. scholarship from European University Cyprus.

## DATA AVAILABILITY

The data underlying this article are available in the article, in public data bases Cornell Atlas of *Spitzer*/Infrared Spectrograph Sources (CASSIS) or are publicly available in the literature.

## REFERENCES

- Antonucci R. R. J., 1993, *ARA&A*, 31, 473
- Antonucci R. R. J., Miller J. S., 1985, *ApJ*, 297, 621
- Armus L. et al., 2009, *PASP*, 121, 559
- Boquien M. et al., 2019, *A&A*, 622, A103
- Braatz J. A. et al., 1993, *ApJ*, 409, L5
- Bruzual G., Charlot S., 1993, *ApJ*, 405, 538
- Bruzual G., Charlot S., 2003, *MNRAS*, 344, 1000
- Byrne C. M. et al., 2022, *MNRAS*, 512, 5329
- Cameron M. et al., 1993, *ApJ*, 419, 136
- Camps P., Baes M., 2020, *Astron. Comput.*, 31, 100381
- Carnall A. C., McLure R. J., Dunlop J. S., Davé R., 2018, *MNRAS*, 480, 4379
- Chevallard J., Charlot S., 2016, *MNRAS*, 462, 1415
- Conroy C., Gunn J. E., White M., 2009, *ApJ*, 699, 486
- da Cunha E., Charlot S., Elbaz D., 2008, *MNRAS*, 388, 1595
- Doore K. et al., 2023, *ApJS*, 266, 39
- Dopita M. A. et al., 2005, *ApJ*, 619, 755
- Draine B. T., Lee H. M., 1984, *ApJ*, 285, 89
- Draine B. T., Li A., 2001, *ApJ*, 551, 807

- Dullemond C. P., van Bemmell I. M., 2005, *A&A*, 436, 47
- Eales S. et al., 2010, *PASP*, 122, 499
- Efstathiou A., 2006, *MNRAS*, 371, L70
- Efstathiou A., Rowan-Robinson M., 1994, *MNRAS*, 266, 212
- Efstathiou A., Rowan-Robinson M., 1995, *MNRAS*, 273, 649
- Efstathiou A., Rowan-Robinson M., 2003, *MNRAS*, 343, 322
- Efstathiou A., Siebenmorgen R., 2009, *A&A*, 502, 541
- Efstathiou A., Hough J. H., Young S., 1995, *MNRAS*, 277, 1134
- Efstathiou A., Rowan-Robinson M., Siebenmorgen R., 2000, *MNRAS*, 313, 734
- Efstathiou A., Christopher N., Verma A., Siebenmorgen R., 2013, *MNRAS*, 436, 1873
- Efstathiou A. et al., 2014, *MNRAS*, 437, L16
- Efstathiou A. et al., 2021, *MNRAS*, 503, L11
- Efstathiou A. et al., 2022, *MNRAS*, 512, 5183
- Eldridge J. J. et al., 2017, *Publ. Astron. Soc. Austr.*, 34, e058
- Endsley R. et al., 2022, *MNRAS*, 512, 4248
- Eufrazio R. T., 2017, Astrophysics Source Code Library, record ascl:1711.009
- Farrah D. et al., 2002, *MNRAS*, 335, 1163
- Farrah D. et al., 2003, *MNRAS*, 343, 585
- Farrah D. et al., 2013, *ApJ*, 776, 38
- Fischer J. et al., 2010, *A&A*, 518, L41
- Foreman-Mackey D., Hogg D. W., Lang D., Goodman J., 2013, *PASP*, 125, 306
- Fritz J., Franceschini A., Hatziminaoglou E., 2006, *MNRAS*, 366, 767
- García-Bernete I. et al., 2024, *A&A*, 681, L7
- González-Alfonso E. et al., 2013, *A&A*, 550, A25
- Goodman J., Weare J., 2010, *Commun. Appl. Math. Comput. Sci.*, 5, 65
- Granato G. L., Danese L., 1994, *MNRAS*, 268, 235
- Groves B. et al., 2008, *ApJS*, 176, 438
- Hailey-Dunsheath S. et al., 2012, *ApJ*, 755, 57
- Hensley B. S., Draine B. T., 2023, *ApJ*, 948, 55
- Herrero-Illana R. et al., 2017, *MNRAS*, 471, 1634
- Heymann F., Siebenmorgen R., 2012, *ApJ*, 751, 27
- Hönig S. F., Kishimoto M., 2017, *ApJ*, 838, L20
- Hönig S. F. et al., 2006, *A&A*, 452, 459
- Houck J. R. et al., 2004, *ApJS*, 154, 18
- Jiang J., Baker W., Young A., Gallo L., 2024, *MNRAS*, 528, 1223
- Johnson S. P., Wilson G. W., Tang Y., Scott K. S., 2013, *MNRAS*, 436, 2535
- Johnson B. D., Leja J., Conroy C., Speagle J. S., 2021, *ApJS*, 254, 22
- Jones A. P. et al., 2017, *A&A*, 602, A46
- Kankare E. et al., 2021, *A&A*, 649, A134
- Kool E. C. et al., 2018, *MNRAS*, 473, 5641
- Krügel E., Siebenmorgen R., 1994, *A&A*, 282, 407
- Lacey C. G. et al., 2016, *MNRAS*, 462, 3854
- Lewis A., 2015, Available at: <http://cosmologist.info/notes/GetDist.pdf>
- Li A., Draine B. T., 2001, *ApJ*, 554, 778
- Li A., Draine B. T., 2002, *ApJ*, 576, 762
- Lonsdale C. J. et al., 2003, *PASP*, 115, 897
- Lonsdale C. J. et al., 2015, *ApJ*, 813, 45
- Maraston C., 2005, *MNRAS*, 362, 799
- Mattila S. et al., 2018, *Science*, 361, 482
- Nenkova M., Ivezić Ž., Elitzur M., 2002, *ApJ*, 570, L9
- Nenkova M., Sirocky M. M., Ivezić Ž., Elitzur M., 2008, *ApJ*, 685, 147
- Noll S. et al., 2009, *A&A*, 507, 1793
- Oliver S. J. et al., 2012, *MNRAS*, 424, 1614
- Pacifici C., Iyer K. G. et al., 2023, *ApJ*, 944, 141
- Paspaliaris E.-D. et al., 2021, *A&A*, 649, A137
- Pier E. A., Krolik J. H., 1992, *ApJ*, 401, 99
- Pier E. A., Krolik J. H., 1993, *ApJ*, 418, 673
- Pitchford L. K. et al., 2019, *MNRAS*, 487, 3130
- Popescu C. C. et al., 2000, *A&A*, 362, 138
- Popescu C. C. et al., 2011, *A&A*, 527, A109
- Popescu C. C. et al., 2017, *MNRAS*, 470, 2539
- Reynolds T. M. et al., 2022, *A&A*, 664, A158
- Rowan-Robinson M., Crawford J., 1989, *MNRAS*, 238, 523
- Rowan-Robinson M., Efstathiou A., 1993, *MNRAS*, 263, 675
- Rowan-Robinson M. et al., 1993, *MNRAS*, 261, 513
- Saunders W. et al., 2000, *MNRAS*, 317, 55
- Schartmann M. et al., 2008, *A&A*, 482, 67
- Shirley R. et al., 2019, *MNRAS*, 490, 634
- Shirley R. et al., 2021, *MNRAS*, 507, 129
- Siebenmorgen R., Krügel E., 1992, *A&A*, 259, 614
- Siebenmorgen R., Krügel E., 2007, *A&A*, 461, 445
- Siebenmorgen R., Heymann F., Efstathiou A., 2015, *A&A*, 583, A120
- Silva L., Granato G. L., Bressan A., Danese L., 1998, *ApJ*, 509, 103
- Speagle J. S., Steinhardt C. L., Capak P. L., Silverman J. D., 2014, *ApJS*, 214, 15
- Stalevski M. et al., 2012, *MNRAS*, 420, 2756
- Stalevski M. et al., 2016, *MNRAS*, 458, 2288
- Sturm E. et al., 2011, *ApJ*, 733, L16
- Takagi T., Arimoto N., Hanami H., 2003, *MNRAS*, 340, 813
- U V. et al., 2012, *ApJS*, 203, 9
- Vega O. et al., 2008, *A&A*, 484, 631
- Verma A. et al., 2002, *MNRAS*, 335, 574
- Yang G. et al., 2020, *MNRAS*, 491, 740
- Yang G. et al., 2022, *ApJ*, 927, 192
- Young S. et al., 1996, *MNRAS*, 281, 1206

## APPENDIX A: PLOTS AND OTHER SED FITTING RESULTS DISCUSSED IN THE PAPER

In this Appendix we give the plots of all of the SED fits with the CYGNUS models, as well as their residuals, for the HERUS sample. We also give two tables with the best-fitting parameters for the fits with the CYGNUS models for the HERUS sample. In addition, we provide tables with extracted physical quantities of the fits of IRAS 08572+3915, VV 340a, and HELP\_J100156.75+022344.7.



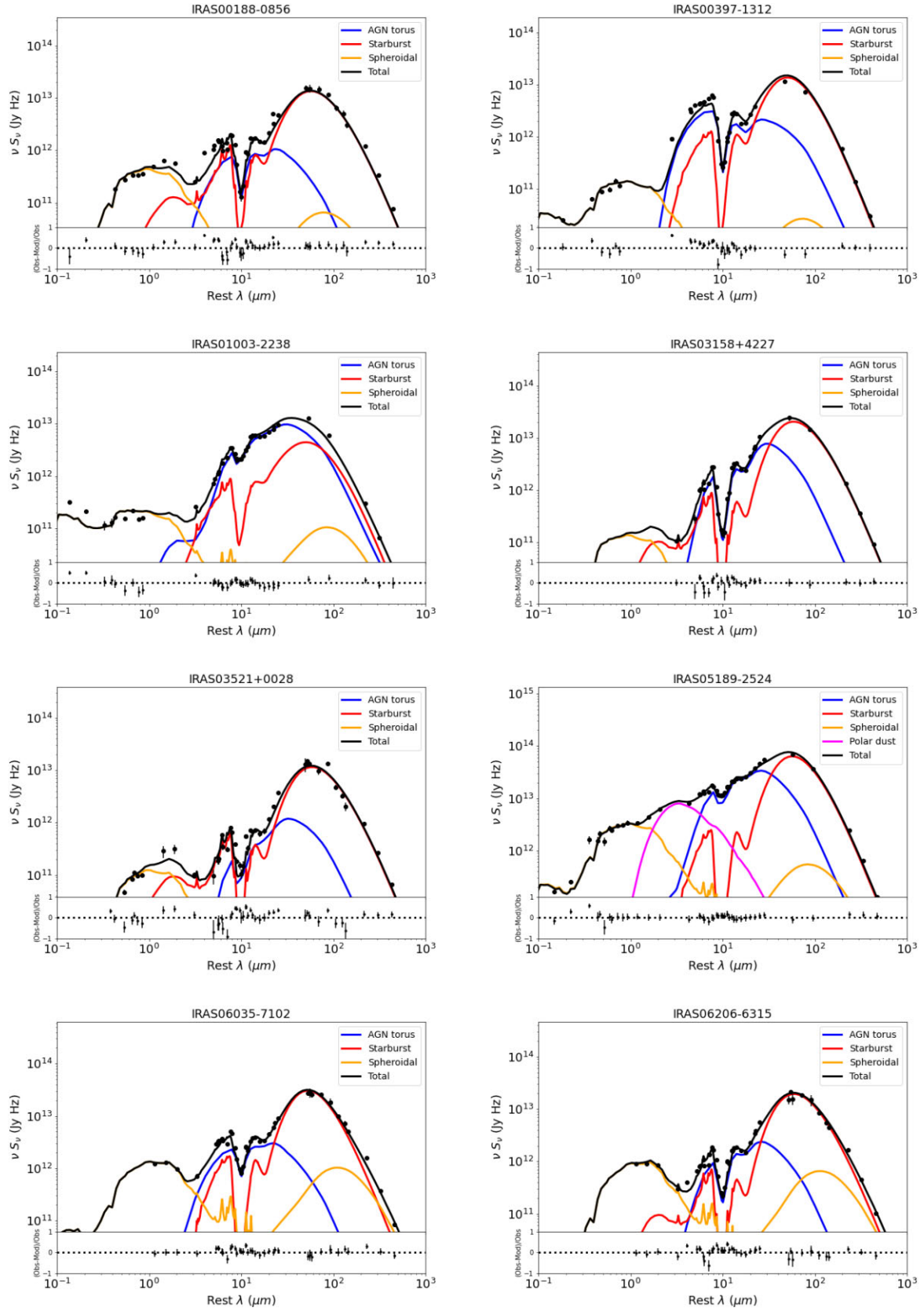


**Figure A1.** SED fit plots of the first eight objects from the list of the HERUS sample, using the CYGNUS models. The AGN torus, starburst, spheroidal host, polar dust and total emission are plotted as shown in the legend.

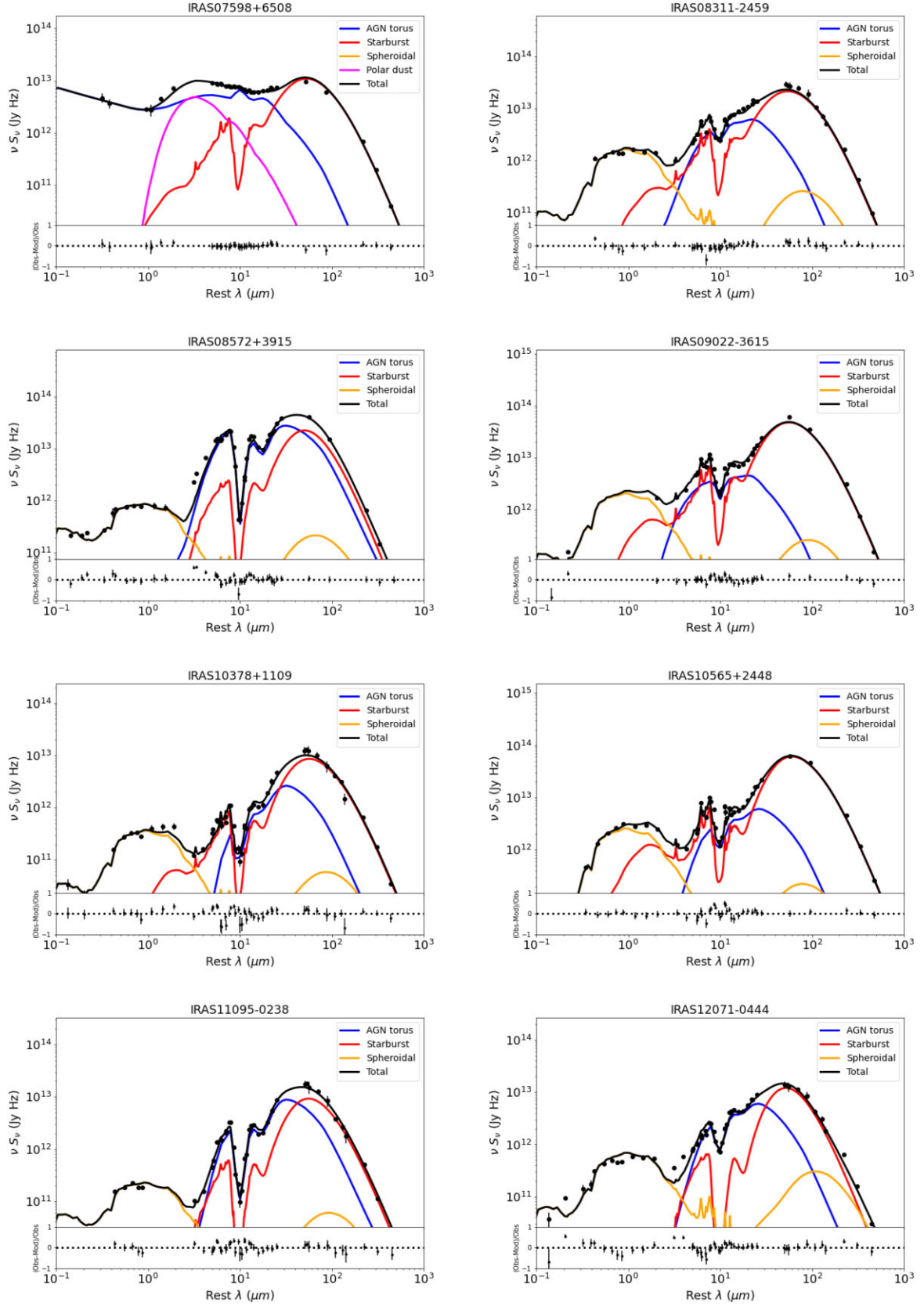


**Figure A2.** SED fit plots of the second eight objects from the list of the HERUS sample, using the CYGNUS models. The AGN torus, starburst, spheroidal host, polar dust and total emission are plotted as shown in the legend.

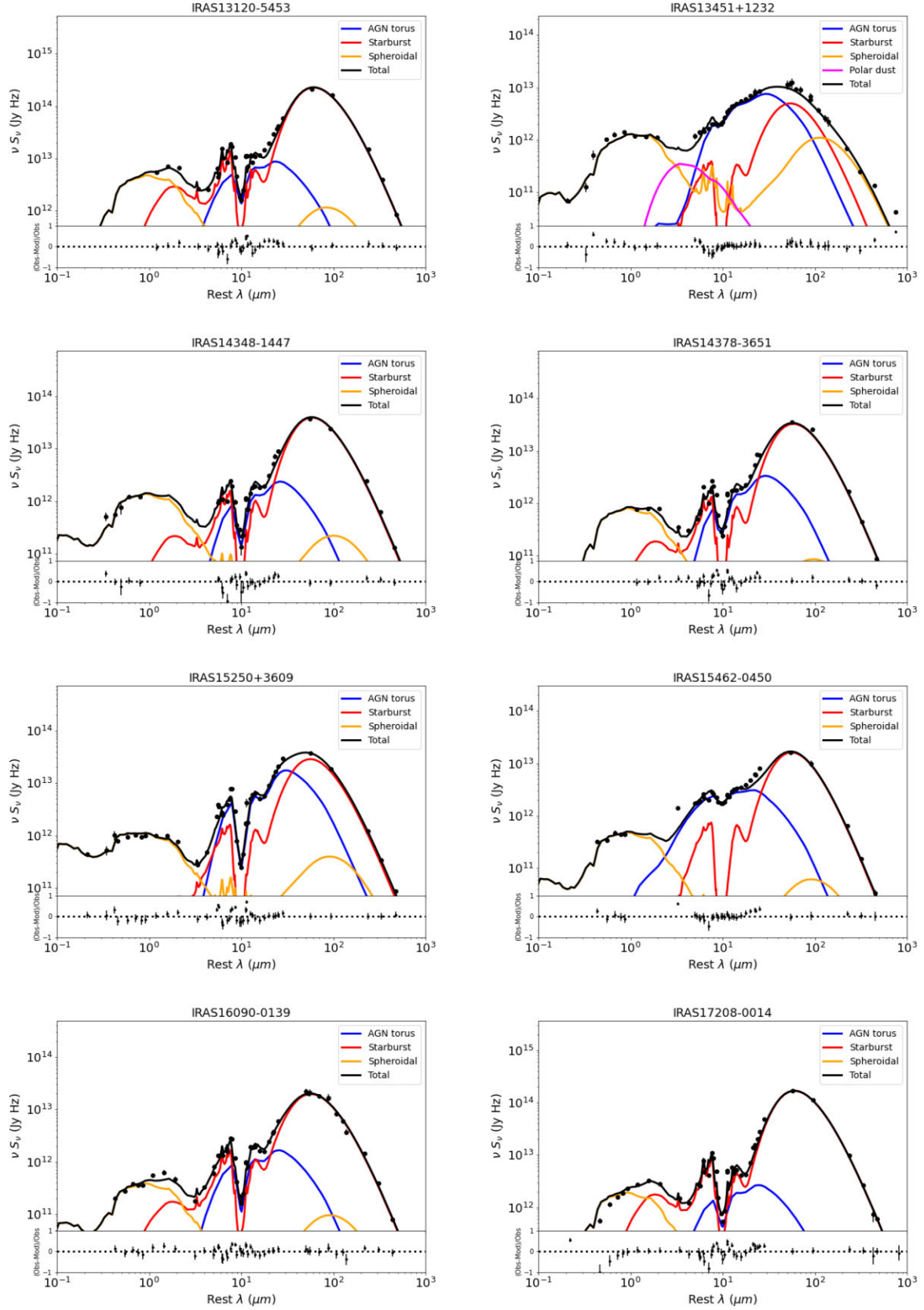


**Figure A3.** SED fit plots of the third eight objects from the list of the HERUS sample, using the CYGNUS models. The AGN torus, starburst, spheroidal host, polar dust and total emission are plotted as shown in the legend.

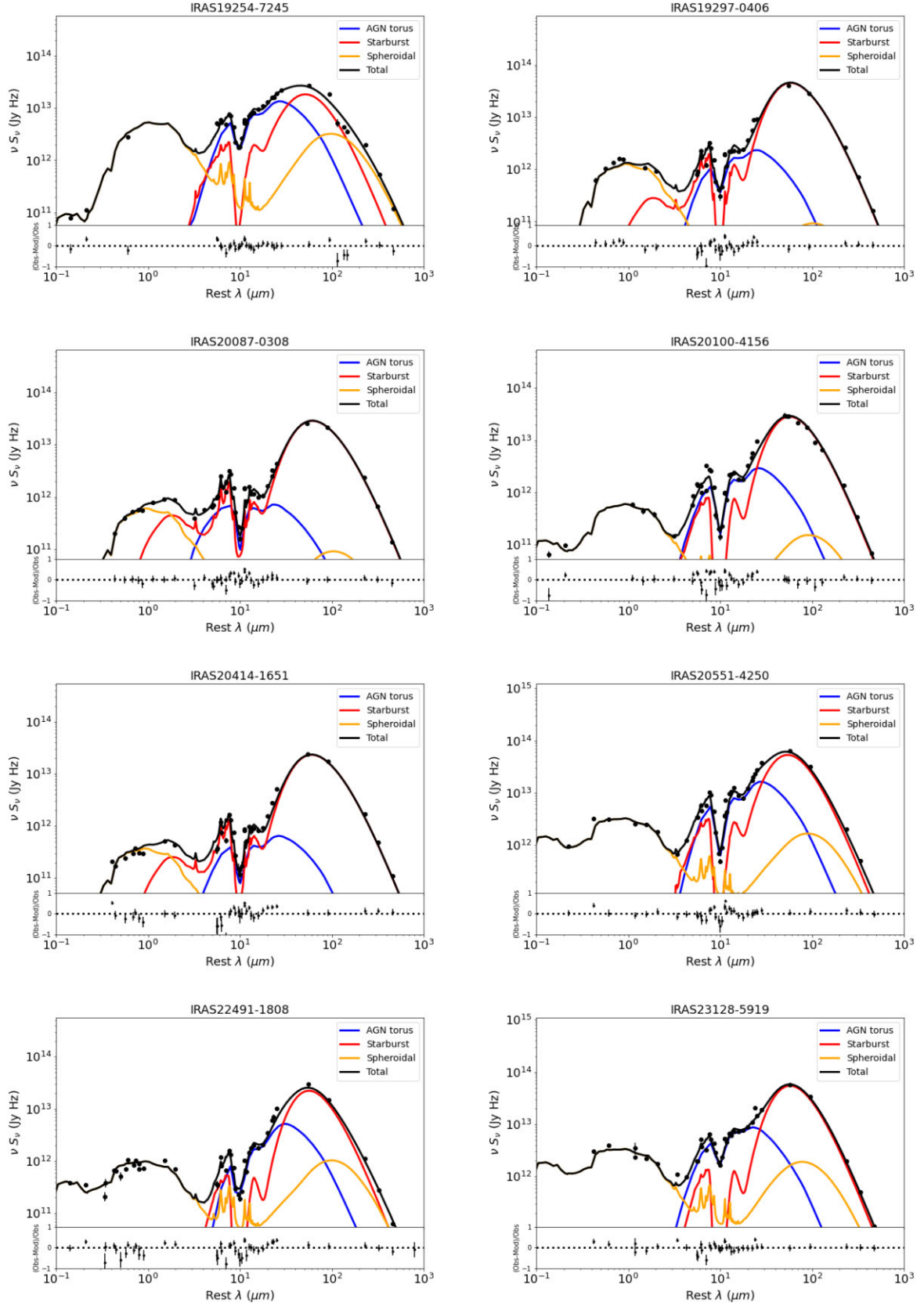


**Figure A4.** SED fit plots of the fourth 8 objects from the list of the HERUS sample, using the CYGNUS models. The AGN torus, starburst, spheroidal host and total emission are plotted as shown in the legend.



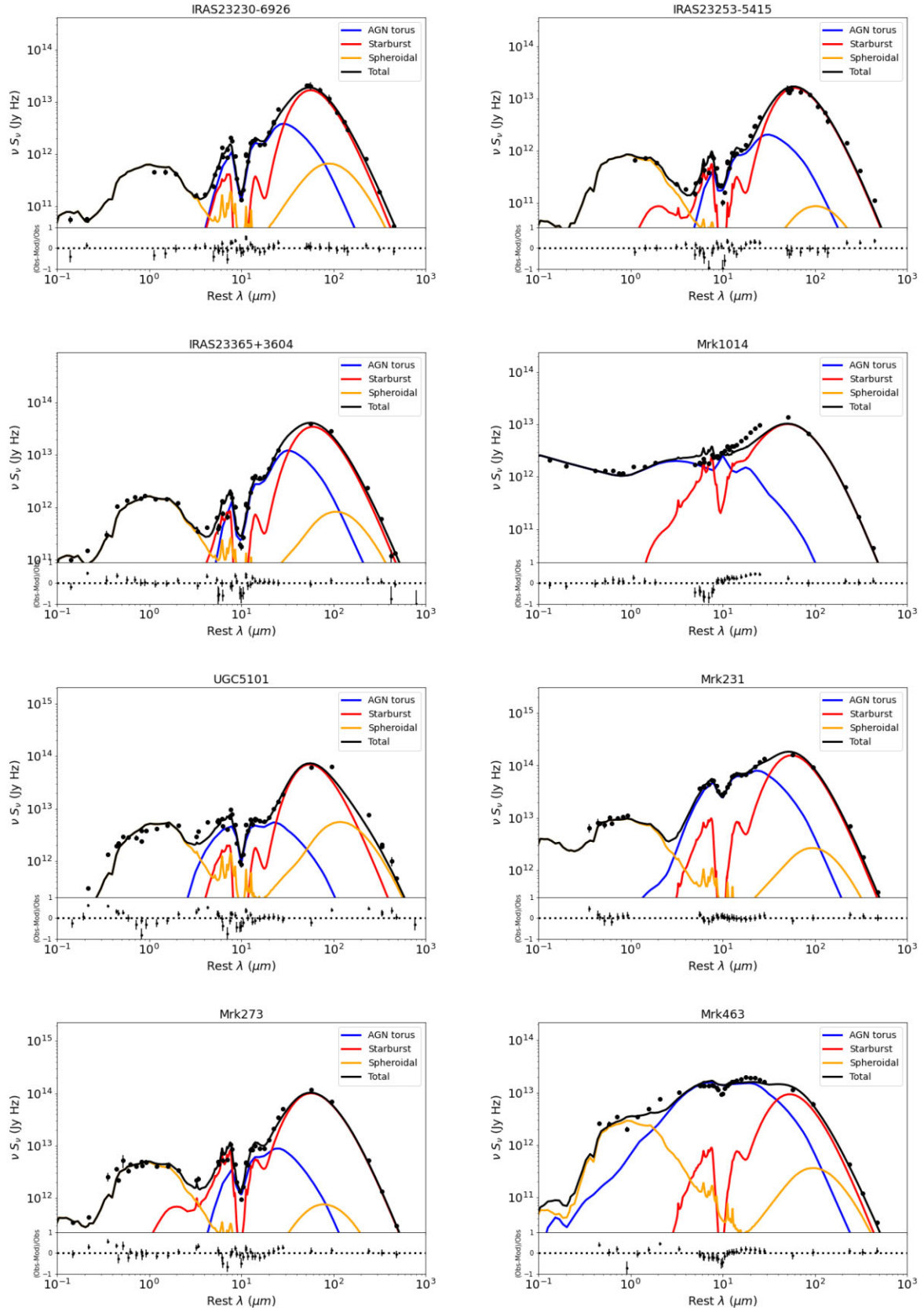


**Figure A5.** SED fit plots of the fifth eight objects from the list of the HERUS sample, using the CYGNUS models. The AGN torus, starburst, spheroidal host and total emission are plotted as shown in the legend.

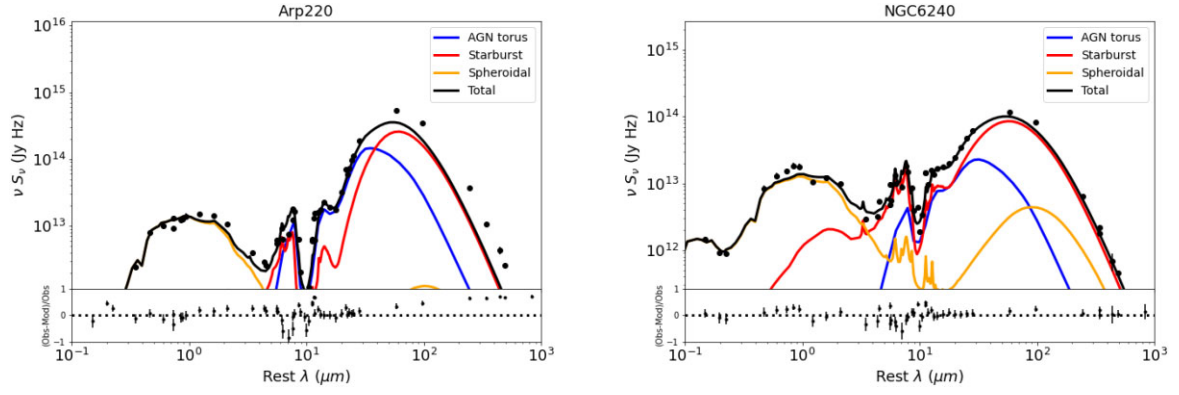


**Figure A6.** SED fit plots of the last two objects from the list of the HERUS sample, using the CYGNUS models. The AGN torus, starburst, spheroidal host and total emission are plotted as shown in the legend. The AGN torus, starburst, spheroidal host and total emission are plotted as shown in the legend.

**Table A1.** Reduced  $\chi^2$  and selected fitted parameters for the galaxies in the HERUS sample.

Name	$z$	$\chi^2_{min,v}$	$\tau_v^s$	$\psi^s$	$\tau^s (10^7 \text{ yr})$	$\tau_v$
IRAS00188–0856	0.12840001	2.66	$1.23^{11.34}_{-0.61}$	$5.59^{0.88}_{-0.92}$	$147.11^{60.13}_{-9.47}$	$128.66^{9.16}_{-17.77}$
IRAS00397–1312	0.2617	2.78	$0.44^{0.54}_{-0.24}$	$8.92^{6.17}_{-2.37}$	$326.65^{50.05}_{-65.95}$	$105.47^{5.39}_{-3.12}$
IRAS01003–2238	0.1178	1.3	$0.77^{0.17}_{-0.36}$	$2.56^{0.4}_{-0.4}$	$778.94^{6.75}_{-29.1}$	$65.58^{4.93}_{-7.73}$
IRAS03158+4227	0.1344	1.64	$0.44^{0.67}_{-0.2}$	$3.07^{2.46}_{-1.15}$	$178.15^{208.11}_{-127.35}$	$186.57^{12.27}_{-14.86}$
IRAS03521+0028	0.1519	3.16	$4.42^{4.06}_{-1.95}$	$2.28^{0.9}_{-0.45}$	$25.37^{3.22}_{-4.22}$	$179.99^{14.26}_{-15.5}$
IRAS05189–2524	0.04256	0.89	$0.91^{0.45}_{-0.23}$	$6.18^{1.3}_{-1.44}$	$166.31^{3.02}_{-5.19}$	$176.84^{12.32}_{-17.3}$
IRAS06035–7102	0.07947	0.87	$9.24^{1.4}_{-5.56}$	$3.7^{0.86}_{-0.28}$	$205.86^{42.66}_{-174.51}$	$144.96^{17.3}_{-51.06}$
IRAS06206–6315	0.09244	1.38	$12.13^{2.21}_{-5.39}$	$3.22^{0.89}_{-0.54}$	$78.51^{16.17}_{-30.69}$	$213.4^{13.74}_{-9.43}$
IRAS07598+6508	0.1483	0.22	$1.0^{1.7}_{-0.59}$	$4.98^{5.59}_{-2.37}$	$96.56^{170.51}_{-60.04}$	$74.93^{13.3}_{-10.46}$
IRAS08311–2459	0.1004	0.74	$1.18^{0.84}_{-0.49}$	$5.07^{2.71}_{-1.28}$	$165.17^{128.78}_{-60.21}$	$69.34^{11.08}_{-10.11}$
IRAS08572+3915	0.05835	1.67	$0.40^{0.36}_{-0.15}$	$10.43^{3.39}_{-2.12}$	$443.13^{36.46}_{-43.89}$	$95.82^{8.98}_{-11.97}$
IRAS09022–3615	0.05964	0.94	$0.67^{0.39}_{-0.28}$	$3.34^{1.99}_{-0.96}$	$164.3^{9.07}_{-7.83}$	$95.28^{11.97}_{-9.54}$
IRAS10378+1109	0.1362	1.65	$1.14^{1.57}_{-0.45}$	$3.91^{1.86}_{-1.08}$	$182.55^{33.44}_{-6.78}$	$121.63^{5.69}_{-7.35}$
IRAS10565+2448	0.043	1.69	$0.47^{0.41}_{-0.18}$	$5.68^{1.36}_{-1.68}$	$85.35^{16.82}_{-14.77}$	$142.66^{3.79}_{-3.43}$
IRAS11095–0238	0.1066	1.22	$1.34^{5.09}_{-0.82}$	$3.54^{1.66}_{-1.67}$	$390.54^{211.33}_{-160.73}$	$140.62^{23.68}_{-12.75}$
IRAS12071–0444	0.1284	1.67	$4.26^{1.58}_{-1.35}$	$1.55^{0.25}_{-0.44}$	$228.69^{95.08}_{-13.62}$	$142.81^{15.37}_{-19.74}$
IRAS13120–5453	0.03076	2.08	$2.48^{2.31}_{-1.49}$	$4.46^{1.95}_{-1.22}$	$184.21^{140.39}_{-89.49}$	$197.84^{1.39}_{-5.12}$
IRAS13451+1232	0.1217	1.84	$8.19^{1.21}_{-0.61}$	$1.67^{0.08}_{-0.21}$	$322.61^{35.84}_{-67.3}$	$130.6^{4.76}_{-8.16}$
IRAS14348–1447	0.0827	2.24	$0.73^{1.26}_{-0.31}$	$3.77^{1.1}_{-1.0}$	$209.25^{70.78}_{-90.79}$	$199.34^{11.04}_{-2.2}$
IRAS14378–3651	0.0676	2.65	$0.83^{6.02}_{-0.54}$	$3.38^{2.09}_{-0.94}$	$114.47^{82.42}_{-26.81}$	$198.56^{26.58}_{-3.49}$
IRAS15250+3609	0.05516	2.31	$0.5^{0.94}_{-0.3}$	$2.1^{0.56}_{-0.34}$	$650.13^{69.35}_{-44.14}$	$153.97^{8.23}_{-7.16}$
IRAS15462–0450	0.09979	1.39	$0.27^{0.43}_{-0.16}$	$2.91^{1.1}_{-1.26}$	$187.39^{161.35}_{-53.98}$	$166.57^{16.86}_{-34.6}$
IRAS16090–0139	0.13358	1.01	$1.72^{6.2}_{-1.39}$	$4.42^{1.19}_{-1.49}$	$305.63^{326.12}_{-265.3}$	$136.43^{5.64}_{-5.3}$
IRAS17208–0014	0.0428	2.55	$0.18^{0.02}_{-0.04}$	$1.14^{0.22}_{-0.01}$	$166.87^{66.33}_{-10.54}$	$198.93^{6.62}_{-0.24}$
IRAS19254–7245	0.061709	1.6	$8.24^{2.27}_{-1.21}$	$4.23^{2.07}_{-1.2}$	$154.04^{5.2}_{-11.84}$	$95.37^{25.1}_{-21.62}$
IRAS19297–0406	0.08573	2.21	$0.28^{0.41}_{-0.14}$	$3.82^{1.7}_{-1.28}$	$70.94^{68.06}_{-38.8}$	$195.56^{2.9}_{-5.88}$
IRAS20087–0308	0.10567	1.5	$2.54^{1.06}_{-1.19}$	$1.9^{1.19}_{-0.54}$	$67.56^{48.77}_{-29.36}$	$196.41^{2.76}_{-3.16}$
IRAS20100–4156	0.12958	2.54	$1.58^{3.11}_{-0.96}$	$4.19^{1.38}_{-1.47}$	$335.05^{104.17}_{-60.68}$	$198.37^{5.41}_{-7.53}$
IRAS20414–1651	0.087084	2.96	$0.14^{0.04}_{-0.02}$	$9.49^{3.49}_{-0.72}$	$165.1^{31.41}_{-9.71}$	$194.78^{4.1}_{-8.12}$
IRAS20551–4250	0.042996	1.77	$2.03^{0.6}_{-0.34}$	$2.83^{1.25}_{-0.69}$	$636.41^{49.67}_{-44.28}$	$147.0^{11.2}_{-10.93}$
IRAS22491–1808	0.0778	2.01	$4.23^{0.22}_{-3.36}$	$1.89^{0.71}_{-0.23}$	$734.86^{25.11}_{-157.92}$	$223.09^{15.12}_{-17.16}$
IRAS23128–5919	0.0446	1.33	$1.87^{1.86}_{-0.98}$	$4.61^{0.48}_{-0.64}$	$698.76^{65.73}_{-111.18}$	$227.74^{13.42}_{-7.57}$
IRAS23230–6926	0.10659	1.98	$7.75^{0.65}_{-1.19}$	$4.4^{1.88}_{-1.11}$	$478.09^{39.74}_{-69.79}$	$218.79^{15.4}_{-15.51}$
IRAS23253–5415	0.13	2.13	$0.18^{0.07}_{-0.04}$	$1.52^{0.33}_{-0.26}$	$149.77^{65.7}_{-51.19}$	$242.16^{3.92}_{-10.16}$
IRAS23365+3604	0.0645	3.09	$5.63^{0.94}_{-4.44}$	$2.67^{0.07}_{-0.18}$	$210.06^{54.53}_{-36.89}$	$229.65^{8.56}_{-6.56}$
Mrk1014	0.16311	2.62	$1.73^{2.48}_{-0.52}$	$3.57^{4.03}_{-1.21}$	$227.58^{168.96}_{-129.66}$	$52.81^{4.86}_{-0.99}$
UGC5101	0.039367	2.93	$13.93^{0.5}_{-0.54}$	$1.37^{0.1}_{-0.12}$	$196.75^{3.92}_{-5.63}$	$196.66^{4.3}_{-5.78}$
Mrk231	0.04217	0.58	$0.57^{0.5}_{-0.41}$	$2.31^{1.14}_{-0.79}$	$514.11^{185.21}_{-157.76}$	$145.48^{36.66}_{-14.34}$
Mrk273	0.03778	1.63	$0.95^{0.38}_{-0.26}$	$5.02^{0.77}_{-1.21}$	$175.69^{4.72}_{-8.87}$	$135.74^{15.82}_{-5.76}$
Mrk463	0.050355	1.5	$1.32^{0.36}_{-0.45}$	$3.4^{0.09}_{-0.92}$	$116.4^{67.27}_{-21.8}$	$116.17^{16.08}_{-11.1}$
Arp220	0.018	5.23	$0.12^{0.03}_{-0.02}$	$1.83^{0.53}_{-0.39}$	$124.13^{1.71}_{-0.22}$	$246.08^{2.19}_{-1.06}$
NGC6240	0.0244	1.62	$3.23^{0.8}_{-1.16}$	$3.96^{0.6}_{-0.24}$	$247.7^{19.01}_{-37.22}$	$76.64^{6.67}_{-6.98}$

**Table A2.** Other fitted parameters for the galaxies in the HERUS sample.

Name	$t_*$ ( $10^7$ yr)	$\tau_*$ ( $10^7$ yr)	$r_2/r_1$	$\tau_{uv}$	$\theta_o$ ( $^\circ$ )	$\theta_i$ ( $^\circ$ )	$T_p$
IRAS00188–0856	$3.22^{+0.08}_{-0.19}$	$1.55^{+0.1}_{-0.05}$	$57.42^{+30.87}_{-21.08}$	$394.96^{+77.68}_{-18.89}$	$46.42^{+2.66}_{-3.95}$	$76.46^{+4.46}_{-0.37}$	–
IRAS00397–1312	$0.77^{+0.14}_{-0.16}$	$2.01^{+0.22}_{-0.23}$	$89.46^{+6.71}_{-5.84}$	$329.52^{+9.58}_{-9.24}$	$73.81^{+0.27}_{-0.09}$	$83.12^{+1.11}_{-0.87}$	–
IRAS01003–2238	$1.38^{+0.25}_{-0.19}$	$1.45^{+0.28}_{-0.11}$	$52.48^{+5.82}_{-3.25}$	$1310.68^{+86.96}_{-24.24}$	$61.37^{+0.19}_{-0.09}$	$69.32^{+0.27}_{-0.2}$	–
IRAS03158+4227	$3.03^{+0.25}_{-0.39}$	$1.39^{+0.15}_{-0.15}$	$30.93^{+5.92}_{-3.6}$	$959.57^{+33.8}_{-51.93}$	$53.97^{+4.84}_{-2.01}$	$76.88^{+0.62}_{-0.6}$	–
IRAS03521+0028	$3.4^{+0.07}_{-0.05}$	$1.55^{+0.2}_{-0.2}$	$45.37^{+1.6}_{-3.74}$	$1245.22^{+81.44}_{-99.23}$	$58.93^{+5.52}_{-3.74}$	$70.52^{+1.82}_{-1.4}$	–
IRAS05189–2524	$2.15^{+0.42}_{-0.28}$	$2.09^{+0.21}_{-0.37}$	$38.24^{+4.1}_{-4.16}$	$911.92^{+72.26}_{-33.33}$	$52.28^{+3.43}_{-1.28}$	$63.61^{+1.75}_{-0.6}$	$1050.6^{+28.7}_{-23.2}$
IRAS06035–7102	$0.84^{+1.99}_{-0.14}$	$2.03^{+0.12}_{-0.43}$	$43.38^{+9.55}_{-4.72}$	$361.74^{+106.82}_{-22.29}$	$48.28^{+1.82}_{-8.36}$	$68.39^{+2.01}_{-2.32}$	–
IRAS06206–6315	$3.09^{+0.2}_{-0.19}$	$1.38^{+0.11}_{-0.11}$	$48.27^{+4.85}_{-5.79}$	$695.61^{+36.17}_{-84.44}$	$45.32^{+4.21}_{-3.83}$	$70.29^{+1.12}_{-1.09}$	–
IRAS07598+6508	$2.83^{+0.2}_{-0.52}$	$2.08^{+0.47}_{-0.4}$	$36.43^{+16.48}_{-10.28}$	$723.81^{+145.32}_{-106.6}$	$63.02^{+2.3}_{-1.76}$	$15.27^{+2.16}_{-2.84}$	$1094.2^{+72.0}_{-98.8}$
IRAS08311–2459	$2.84^{+0.15}_{-0.12}$	$1.22^{+0.23}_{-0.11}$	$30.23^{+6.94}_{-3.93}$	$650.82^{+97.1}_{-82.22}$	$48.54^{+4.38}_{-3.8}$	$60.15^{+2.95}_{-1.86}$	–
IRAS08572+3915	$0.64^{+0.28}_{-0.1}$	$1.79^{+0.34}_{-0.25}$	$58.5^{+9.8}_{-8.38}$	$612.99^{+14.44}_{-21.13}$	$72.66^{+1.05}_{-0.89}$	$79.04^{+0.74}_{-0.65}$	–
IRAS09022–3615	$3.08^{+0.24}_{-0.2}$	$1.41^{+0.12}_{-0.25}$	$40.44^{+8.88}_{-7.7}$	$308.95^{+38.16}_{-30.87}$	$37.15^{+3.16}_{-8.14}$	$63.27^{+2.77}_{-3.59}$	–
IRAS10378+1109	$2.98^{+0.3}_{-0.22}$	$1.3^{+0.35}_{-0.14}$	$31.19^{+7.18}_{-5.31}$	$1427.8^{+51.92}_{-135.04}$	$51.29^{+1.97}_{-2.56}$	$72.63^{+0.81}_{-2.14}$	–
IRAS10565+2448	$3.47^{+0.02}_{-0.02}$	$1.05^{+0.05}_{-0.04}$	$44.7^{+5.66}_{-5.41}$	$825.07^{+38.72}_{-59.02}$	$54.12^{+2.16}_{-1.54}$	$66.1^{+0.6}_{-0.75}$	–
IRAS11095–0238	$2.46^{+0.81}_{-1.25}$	$1.92^{+0.57}_{-0.38}$	$59.51^{+11.12}_{-16.98}$	$904.31^{+53.4}_{-37.8}$	$60.14^{+2.46}_{-3.65}$	$76.33^{+0.79}_{-0.89}$	–
IRAS12071–0444	$0.63^{+0.31}_{-0.12}$	$1.88^{+0.02}_{-0.1}$	$38.36^{+0.69}_{-2.4}$	$794.25^{+24.03}_{-30.22}$	$47.29^{+0.2}_{-3.41}$	$66.95^{+0.48}_{-0.8}$	–
IRAS13120–5453	$3.38^{+0.08}_{-0.06}$	$1.05^{+0.06}_{-0.02}$	$51.96^{+3.76}_{-5.55}$	$554.66^{+9.27}_{-41.27}$	$43.12^{+5.92}_{-1.56}$	$67.39^{+0.75}_{-2.69}$	–
IRAS13451+1232	$1.49^{+0.03}_{-0.15}$	$1.49^{+0.15}_{-0.17}$	$39.07^{+5.08}_{-3.41}$	$1456.38^{+19.18}_{-42.13}$	$51.33^{+0.54}_{-2.2}$	$64.28^{+0.35}_{-1.55}$	$938.9^{+33.3}_{-13.2}$
IRAS14348–1447	$3.39^{+0.07}_{-0.16}$	$2.16^{+0.28}_{-0.23}$	$25.75^{+3.24}_{-2.71}$	$802.79^{+96.15}_{-140.11}$	$51.38^{+4.0}_{-3.78}$	$70.64^{+1.35}_{-1.71}$	–
IRAS14378–3651	$3.43^{+0.04}_{-0.03}$	$2.26^{+0.23}_{-0.58}$	$43.77^{+14.34}_{-4.42}$	$1035.7^{+252.4}_{-114.91}$	$47.17^{+4.29}_{-3.19}$	$68.96^{+1.95}_{-0.61}$	–
IRAS15250+3609	$2.99^{+0.36}_{-0.64}$	$2.87^{+0.32}_{-0.4}$	$34.51^{+2.53}_{-2.87}$	$927.48^{+26.0}_{-29.82}$	$55.78^{+1.06}_{-1.94}$	$76.97^{+0.82}_{-0.49}$	–
IRAS15462–0450	$1.87^{+0.59}_{-0.55}$	$2.25^{+0.52}_{-0.32}$	$38.77^{+17.9}_{-6.05}$	$532.12^{+78.8}_{-55.67}$	$55.53^{+7.7}_{-1.2}$	$60.96^{+3.81}_{-1.62}$	–
IRAS16090–0139	$3.44^{+0.04}_{-0.08}$	$2.01^{+0.25}_{-0.31}$	$46.52^{+4.75}_{-3.4}$	$545.12^{+49.17}_{-24.69}$	$46.62^{+6.14}_{-3.44}$	$72.82^{+1.55}_{-1.13}$	–
IRAS17208–0014	$3.44^{+0.0}_{-0.04}$	$1.32^{+0.01}_{-0.03}$	$46.3^{+2.02}_{-1.23}$	$633.32^{+1.29}_{-16.95}$	$48.08^{+3.57}_{-2.53}$	$65.94^{+0.29}_{-0.44}$	–
IRAS19254–7245	$1.13^{+0.13}_{-0.2}$	$2.53^{+0.42}_{-0.45}$	$43.82^{+7.91}_{-4.61}$	$780.52^{+42.86}_{-98.51}$	$55.46^{+2.31}_{-1.32}$	$68.66^{+0.75}_{-0.66}$	–
IRAS19297–0406	$3.44^{+0.01}_{-0.06}$	$2.0^{+0.22}_{-0.5}$	$78.41^{+9.95}_{-23.53}$	$824.04^{+81.58}_{-40.58}$	$41.04^{+2.88}_{-4.01}$	$64.06^{+2.21}_{-1.97}$	–
IRAS20087–0308	$3.48^{+0.01}_{-0.02}$	$1.04^{+0.04}_{-0.03}$	$49.76^{+7.82}_{-4.88}$	$316.83^{+15.92}_{-16.97}$	$58.14^{+1.66}_{-2.27}$	$80.16^{+1.72}_{-2.36}$	–
IRAS20100–4156	$2.0^{+0.45}_{-0.9}$	$2.54^{+0.68}_{-0.72}$	$45.69^{+9.01}_{-5.02}$	$613.02^{+65.63}_{-35.23}$	$47.39^{+3.11}_{-2.75}$	$73.59^{+0.81}_{-0.97}$	–
IRAS20414–1651	$3.4^{+0.04}_{-0.03}$	$1.22^{+0.01}_{-0.04}$	$51.91^{+4.43}_{-5.34}$	$620.3^{+90.57}_{-47.04}$	$62.2^{+0.76}_{-2.88}$	$70.79^{+0.63}_{-0.31}$	–
IRAS20551–4250	$1.26^{+0.36}_{-0.22}$	$1.7^{+0.37}_{-0.49}$	$42.29^{+4.32}_{-4.7}$	$732.36^{+24.46}_{-17.98}$	$48.65^{+2.84}_{-2.31}$	$74.11^{+0.85}_{-1.19}$	–
IRAS22491–1808	$1.46^{+1.79}_{-0.48}$	$2.45^{+0.22}_{-0.3}$	$32.91^{+4.86}_{-4.48}$	$1237.53^{+109.38}_{-59.62}$	$49.02^{+1.98}_{-1.38}$	$71.39^{+0.67}_{-1.71}$	–
IRAS23128–5919	$1.55^{+0.41}_{-0.5}$	$1.21^{+0.1}_{-0.13}$	$31.21^{+3.91}_{-4.0}$	$612.96^{+34.8}_{-35.47}$	$44.41^{+2.01}_{-1.94}$	$63.37^{+0.46}_{-0.81}$	–
IRAS23230–6926	$1.32^{+0.27}_{-0.32}$	$1.58^{+0.28}_{-0.19}$	$45.45^{+5.7}_{-4.53}$	$813.11^{+29.03}_{-36.16}$	$48.57^{+2.3}_{-2.03}$	$74.03^{+0.72}_{-0.7}$	–
IRAS23253–5415	$3.21^{+0.17}_{-0.1}$	$1.39^{+0.45}_{-0.24}$	$93.24^{+2.3}_{-4.69}$	$1378.25^{+41.64}_{-26.05}$	$49.08^{+1.76}_{-1.71}$	$68.78^{+0.59}_{-0.98}$	–
IRAS23365+3604	$2.54^{+0.1}_{-0.18}$	$1.19^{+0.22}_{-0.04}$	$26.41^{+0.51}_{-1.68}$	$1442.99^{+22.88}_{-19.41}$	$51.7^{+2.1}_{-3.48}$	$74.55^{+0.19}_{-0.36}$	–
Mrk1014	$2.13^{+0.2}_{-0.14}$	$1.18^{+0.16}_{-0.13}$	$61.14^{+11.1}_{-9.45}$	$286.33^{+103.28}_{-19.2}$	$59.76^{+1.04}_{-0.85}$	$18.06^{+1.83}_{-1.22}$	–
UGC5101	$1.05^{+0.09}_{-0.06}$	$1.51^{+0.2}_{-0.08}$	$76.09^{+4.28}_{-8.96}$	$339.69^{+22.83}_{-23.61}$	$46.29^{+1.8}_{-2.13}$	$75.48^{+0.22}_{-1.19}$	–
Mrk231	$2.1^{+0.33}_{-0.36}$	$1.52^{+0.14}_{-0.12}$	$40.1^{+4.43}_{-6.97}$	$636.02^{+35.16}_{-22.87}$	$54.24^{+2.76}_{-3.08}$	$63.79^{+1.22}_{-1.03}$	–
Mrk273	$2.98^{+0.12}_{-0.16}$	$1.33^{+0.12}_{-0.08}$	$37.9^{+4.06}_{-1.1}$	$788.22^{+106.94}_{-91.5}$	$44.88^{+1.48}_{-2.48}$	$66.61^{+0.84}_{-1.83}$	–
Mrk463	$1.67^{+0.46}_{-0.38}$	$2.18^{+0.16}_{-0.21}$	$46.87^{+5.6}_{-18.56}$	$517.08^{+68.32}_{-100.63}$	$63.17^{+3.89}_{-1.71}$	$63.26^{+1.56}_{-3.02}$	–
Arp220	$2.95^{+0.04}_{-0.02}$	$1.11^{+0.08}_{-0.07}$	$59.58^{+15.48}_{-7.3}$	$1447.17^{+16.31}_{-4.36}$	$48.24^{+0.27}_{-1.42}$	$78.29^{+0.3}_{-0.57}$	–
NGC6240	$3.23^{+0.18}_{-0.19}$	$1.25^{+0.23}_{-0.16}$	$44.07^{+4.56}_{-7.74}$	$1097.07^{+95.22}_{-76.14}$	$54.62^{+3.61}_{-2.12}$	$71.3^{+0.66}_{-0.67}$	–



**Table A3.** Selected extracted physical quantities for IRAS 08572+3915. For the AGN and total luminosities the anisotropy-corrected luminosities are given.

AGN model	$L_{\text{AGN}}^c$ $10^{12} \text{ L}_{\odot}$	$L_{\text{SB}}$ $10^{11} \text{ L}_{\odot}$	$L_{\text{sph}}$ $10^{10} \text{ L}_{\odot}$	$L_{\text{tot}}^c$ $10^{12} \text{ L}_{\odot}$	$\dot{M}_{*}^{\text{age}}$ $\text{M}_{\odot} \text{ yr}^{-1}$	$\dot{M}_{\text{sph}}$ $\text{M}_{\odot} \text{ yr}^{-1}$
CYGNUS	$12.85_{-1.36}^{+1.1}$	$5.46_{-1.07}^{+0.42}$	$1.67_{-0.09}^{+0.08}$	$13.34_{-1.4}^{+1.21}$	$154.0_{-48.26}^{+17.93}$	$1.52_{-0.13}^{+0.15}$
Fritz et al. (2006)	$4.14_{-0.55}^{+0.0}$	$2.07_{-0.0}^{+3.35}$	$2.73_{-1.0}^{+0.0}$	$4.38_{-0.22}^{+0.0}$	$55.93_{-0.0}^{+75.42}$	$2.31_{-1.56}^{+0.0}$
SKIRTOR	$0.0_{-0.0}^{+0.01}$	$14.35_{-0.21}^{+0.15}$	$1.59_{-0.03}^{+0.1}$	$1.45_{-0.02}^{+0.02}$	$428.1_{-8.14}^{+9.09}$	$1.46_{-0.07}^{+0.1}$
Siebenmorgen et al. (2015)	$0.01_{-0.0}^{+0.01}$	$14.33_{-0.22}^{+0.31}$	$1.57_{-0.05}^{+0.05}$	$1.46_{-0.03}^{+0.03}$	$430.1_{-10.15}^{+6.11}$	$1.42_{-0.07}^{+0.1}$

**Table A4.** Other extracted physical quantities for IRAS 08572+3915.

AGN model	$\dot{M}_{\text{tot}}$ $\text{M}_{\odot} \text{ yr}^{-1}$	$M_{\text{sph}}^*$ $10^{10} \text{ M}_{\odot}$	$M_{\text{SB}}^*$ $10^9 \text{ M}_{\odot}$	$M_{\text{tot}}^*$ $10^{10} \text{ M}_{\odot}$	$F_{\text{AGN}}$	$A$
CYGNUS	$155.5_{-48.19}^{+18.02}$	$2.19_{-0.15}^{+0.19}$	$0.9_{-0.07}^{+0.14}$	$2.28_{-0.16}^{+0.22}$	$0.96_{-0.01}^{+0.01}$	$14.2_{-1.29}^{+1.38}$
Fritz et al. (2006)	$58.24_{-0.0}^{+73.86}$	$2.1_{-0.0}^{+2.28}$	$1.63_{-0.0}^{+0.18}$	$2.27_{-0.0}^{+2.3}$	$0.95_{-0.08}^{+0.0}$	$3.53_{-0.0}^{+0.5}$
SKIRTOR	$429.8_{-8.48}^{+8.91}$	$2.24_{-0.13}^{+0.18}$	$2.11_{-0.03}^{+0.03}$	$2.45_{-0.14}^{+0.18}$	$0.0_{-0.0}^{+0.0}$	$1.4_{-0.36}^{+1.14}$
Siebenmorgen et al. (2015)	$431.5_{-10.09}^{+6.05}$	$2.18_{-0.13}^{+0.14}$	$2.1_{-0.04}^{+0.07}$	$2.4_{-0.14}^{+0.14}$	$0.0_{-0.0}^{+0.0}$	$3.64_{-0.66}^{+0.38}$

**Table A5.** Selected extracted physical quantities for VV 340a. For the AGN and total luminosities the anisotropy-corrected luminosities are given.

Host galaxy model	$L_{\text{AGN}}^c$ $10^{12} \text{ L}_{\odot}$	$L_{\text{SB}}$ $10^{11} \text{ L}_{\odot}$	$L_{\text{sph}}$ or $L_{\text{disc}}$ $10^{10} \text{ L}_{\odot}$	$L_{\text{tot}}^c$ $10^{12} \text{ L}_{\odot}$	$\dot{M}_{*}^{\text{age}}$ $\text{M}_{\odot} \text{ yr}^{-1}$	$\dot{M}_{\text{sph}}$ $\text{M}_{\odot} \text{ yr}^{-1}$
Spheroidal	$0.05_{-0.02}^{+0.01}$	$2.55_{-0.45}^{+0.33}$	$16.12_{-0.55}^{+1.71}$	$0.46_{-0.04}^{+0.05}$	$78.21_{-3.35}^{+36.21}$	$3.81_{-0.62}^{+1.09}$
Disc	$0.25_{-0.04}^{+0.06}$	$1.48_{-0.33}^{+0.23}$	$30.98_{-0.67}^{+2.1}$	$0.72_{-0.03}^{+0.04}$	$35.41_{-8.42}^{+5.26}$	$11.56_{-0.29}^{+1.28}$

**Table A6.** Other extracted physical quantities for VV 340a.

Host galaxy model	$\dot{M}_{\text{tot}}$ $\text{M}_{\odot} \text{ yr}^{-1}$	$M_{\text{sph}}^*$ or $M_{\text{disc}}^*$ $10^{10} \text{ M}_{\odot}$	$M_{\text{SB}}^*$ $10^9 \text{ M}_{\odot}$	$M_{\text{tot}}^*$ $10^{10} \text{ M}_{\odot}$	$F_{\text{AGN}}$	$A$
Spheroidal	$81.98_{-3.32}^{+36.33}$	$21.24_{-1.01}^{+3.99}$	$2.38_{-0.13}^{+0.82}$	$21.47_{-1.0}^{+4.04}$	$0.1_{-0.03}^{+0.02}$	$1.65_{-0.67}^{+0.36}$
Disc	$47.79_{-0.29}^{+4.43}$	$21.34_{-0.49}^{+0.78}$	$0.36_{-0.07}^{+0.03}$	$21.38_{-0.48}^{+0.77}$	$0.35_{-0.04}^{+0.07}$	$8.3_{-0.8}^{+0.84}$

**Table A7.** Selected extracted physical quantities for HELP\_J100156.75+022344.7. For the AGN and total luminosities the anisotropy-corrected luminosities are given.

AGN model	$L_{\text{AGN}}^c$ $10^{12} \text{ L}_{\odot}$	$L_{\text{SB}}$ $10^{11} \text{ L}_{\odot}$	$L_{\text{sph}}$ $10^{10} \text{ L}_{\odot}$	$L_{\text{tot}}^c$ $10^{12} \text{ L}_{\odot}$	$\dot{M}_{*}^{\text{age}}$ $\text{M}_{\odot} \text{ yr}^{-1}$	$\dot{M}_{\text{sph}}$ $\text{M}_{\odot} \text{ yr}^{-1}$
CYGNUS	$23.54_{-5.08}^{+0.24}$	$40.83_{-5.05}^{+4.8}$	$9.88_{-1.78}^{+35.02}$	$27.45_{-4.27}^{+0.28}$	$994.3_{-110.2}^{+86.46}$	$7.29_{-2.58}^{+27.14}$
Fritz et al. (2006)	$14.62_{-1.54}^{+1.28}$	$55.31_{-7.06}^{+7.92}$	$9.7_{-1.59}^{+7.53}$	$20.27_{-1.06}^{+1.15}$	$1349.0_{-204.4}^{+160.7}$	$8.19_{-1.19}^{+4.92}$
SKIRTOR	$15.29_{-1.91}^{+4.65}$	$50.07_{-6.45}^{+12.52}$	$10.62_{-2.96}^{+4.41}$	$20.45_{-2.02}^{+5.35}$	$1267.0_{-206.3}^{+285.3}$	$8.2_{-2.2}^{+3.17}$
Siebenmorgen et al. (2015)	$26.58_{-1.89}^{+5.32}$	$2.27_{-2.22}^{+17.66}$	$9.71_{-1.57}^{+6.72}$	$28.83_{-3.78}^{+3.34}$	$54.48_{-53.2}^{+461.9}$	$8.35_{-1.89}^{+4.4}$

**Table A8.** Other extracted physical quantities for HELP\_J100156.75+022344.7.

AGN model	$\dot{M}_{\text{tot}}$ $\text{M}_{\odot} \text{ yr}^{-1}$	$M_{\text{sph}}^*$ $10^{10} \text{ M}_{\odot}$	$M_{\text{SB}}^*$ $10^9 \text{ M}_{\odot}$	$M_{\text{tot}}^*$ $10^{10} \text{ M}_{\odot}$	$F_{\text{AGN}}$	$A$
CYGNUS	$999.0^{132.2}_{-108.1}$	$4.13^{0.31}_{-0.36}$	$17.57^{0.98}_{-5.36}$	$5.74^{0.23}_{-0.17}$	$0.85^{0.01}_{-0.05}$	$1.22^{0.07}_{-0.04}$
Fritz et al. (2006)	$1357.0^{160.4}_{-196.8}$	$3.41^{0.46}_{-0.39}$	$18.32^{7.54}_{-5.16}$	$5.33^{0.34}_{-0.54}$	$0.72^{0.04}_{-0.03}$	$1.55^{0.07}_{-0.04}$
SKIRTOR	$1273.0^{292.2}_{-203.0}$	$3.71^{0.45}_{-0.27}$	$19.97^{14.84}_{-8.46}$	$5.66^{1.69}_{-0.89}$	$0.74^{0.05}_{-0.04}$	$1.45^{0.24}_{-0.12}$
Siebenmorgen et al. (2015)	$62.2^{464.2}_{-49.23}$	$3.16^{0.32}_{-0.53}$	$0.94^{9.71}_{-0.93}$	$3.18^{1.06}_{-0.21}$	$0.99^{0.0}_{-0.07}$	$1.36^{0.08}_{-0.2}$

This paper has been typeset from a  $\text{\LaTeX}$  file prepared by the author.